

# UC San Diego

## UC San Diego Previously Published Works

### Title

Cardiolipin remodeling maintains the inner mitochondrial membrane in cells with saturated lipidomes.

### Permalink

<https://escholarship.org/uc/item/5vb43775>

### Journal

Journal of Lipid Research, 65(8)

### Authors

Venkatraman, Kailash  
Budin, Itay

### Publication Date

2024-08-01

### DOI

10.1016/j.jlr.2024.100601

Peer reviewed

# Cardiolipin remodeling maintains the inner mitochondrial membrane in cells with saturated lipidomes

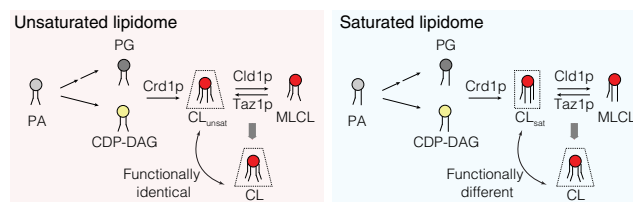
Kailash Venkatraman<sup>1</sup> and Itay Budin<sup>1\*</sup>

Department of Chemistry and Biochemistry, University of California San Diego, La Jolla, CA, USA

**Abstract** Cardiolipin (CL) is a unique, four-chain phospholipid synthesized in the inner mitochondrial membrane (IMM). The acyl chain composition of CL is regulated through a remodeling pathway, whose loss causes mitochondrial dysfunction in Barth syndrome (BTHS). Yeast has been used extensively as a model system to characterize CL metabolism, but mutants lacking its two remodeling enzymes, Cld1p and Taz1p, exhibit mild structural and respiratory phenotypes compared to mammalian cells. Here, we show an essential role for CL remodeling in the structure and function of the IMM in yeast grown under reduced oxygenation. Microaerobic fermentation, which mimics natural yeast environments, caused the accumulation of saturated fatty acids and, under these conditions, remodeling mutants showed a loss of IMM ultrastructure. We extended this observation to HEK293 cells, where phospholipase A<sub>2</sub> inhibition by Bromoenol lactone resulted in respiratory dysfunction and cristae loss upon mild treatment with exogenous saturated fatty acids. In microaerobic yeast, remodeling mutants accumulated unremodeled, saturated CL, but also displayed reduced total CL levels, highlighting the interplay between saturation and CL biosynthesis and/or breakdown. We identified the mitochondrial phospholipase A<sub>1</sub> Ddl1p as a regulator of CL levels, and those of its precursors phosphatidylglycerol and phosphatidic acid, under these conditions. Loss of Ddl1p partially rescued IMM structure in cells unable to initiate CL remodeling and had differing lipidomic effects depending on oxygenation. These results introduce a revised yeast model for investigating CL remodeling and suggest that its structural functions are dependent on the overall lipid environment in the mitochondrion.

**Supplementary key words** mitochondria • phospholipids • cardiolipin • lipid saturation • Barth syndrome

Cardiolipin (CL) is a mitochondrially synthesized phospholipid (PL) whose structure contains two phosphates and four acyl chains. In eukaryotes, CL is synthesized from the condensation of mitochondrial phosphatidylglycerol (PG) and cytidine diphosphate



diacylglycerol (DAG), both of which are derived from phosphatidic acid (PA) that is imported from the endoplasmic reticulum (ER) (1). CL makes specific interactions with electron transport chain (ETC) proteins and their super complexes, which are required for optimal function of the ETC and ATP synthesis (2–5). Depending on its chemical environment, CL can behave as a nonbilayer lipid due to its negative spontaneous curvature (6). Through this property, CL could also function in shaping the morphology of the inner mitochondrial membrane (IMM) (7), particularly its highly curved folds (cristae), and in mitochondrial fission-fusion dynamics (8–12).

The acyl chain composition of CL is determined post-synthetically through a remodeling pathway. In humans, heart CL typically contains four linoleic acid (18:2) chains while in the brain and gut there is a wider distribution of CL acyl chain identities, with oleic acid (18:1, OA) the most common (13–15). Despite this relative heterogeneity, the most abundant form of CL in every organism contains unsaturations on each acyl chain (14, 16). CL acyl chain composition results from the coordinated action of two types of remodeling enzymes, phospholipases and a transacylase, responsible for converting immature CL, which contains saturated chains, to a mature, tetra-unsaturated form of CL (17–20). Phospholipase A<sub>2</sub> (iPLA<sub>2</sub>) enzymes first initiate CL remodeling by deacylation of nascent CL into monolysocardiolipin (MLCL) (21, 22). The transacylase tafazzin (TAZ) then catalyzes the reacylation of MLCL into a homogeneously unsaturated CL by transferring unsaturated acyl chains from mitochondrial PLs (17, 23).

\*For correspondence: Itay Budin, [ibudin@ucsd.edu](mailto:ibudin@ucsd.edu).

Abnormal CL compositions have been linked to human pathologies and are thought to drive mitochondrial dysfunction (24, 25).

CL remodeling is lost in patients with Barth syndrome (BTHS), an X-linked disease which arises from a mutation in the *TAZ* gene (26, 27). BTHS patients have altered CL profiles, characterized by a reduction in CL, and increases in MLCL and unremodeled, saturated CL (28–31). This altered CL composition is thought to cause BTHS-associated mitochondrial defects resulting in cardiac and skeletal muscle myopathies, neutropenia, muscle weakness, and fatigue (32, 33). Multiple model systems show increases in the MLCL:CL ratio upon tafazzin loss (21, 34–37), and BTHS diagnosis is often performed by assessment of this ratio (38). Identification of the negative impacts of MLCL in mitochondrial membranes has led to therapeutic efforts to prevent its formation. This has been achieved through treatment with bromoenol lactone (BEL), an iPLA<sub>2</sub> inhibitor (39). BEL mitigates the MLCL:CL ratio in patient lymphoblasts and stabilizes ETC complexes in HEK293 models of BTHS (21, 40). However, despite the reduction in MLCL, BEL-treated cells do not recover respiratory function to control levels (36). Thus, it remains unclear if MLCL is the only molecular driver of mitochondrial dysfunction in BTHS. Notably, BEL-treated cells still accumulate unremodeled CL (22), whose contribution to respiratory and morphological defects have yet to be shown in mammalian mitochondria independently of MLCL.

Budding yeast (*Saccharomyces cerevisiae*) has been used extensively as a model system to investigate CL remodeling and cellular mechanisms underlying BTHS (37, 41). While mammals contain multiple CL remodeling processes (24), yeast only perform tafazzin-mediated remodeling. Unlike mammalian cells, yeast mutants in the CL synthesis and remodeling pathway have considerably milder phenotypes. In yeast, a single phospholipase A<sub>2</sub> (Cldlp), conducts the deacylation of nascent CL to MLCL (42). Tafazzin (Tazlp) then transfers an unsaturated acyl chain from mitochondrial phosphatidylcholine (PC) to CL to make tetraoleoyl (18:1) cardiolipin (TOCL) (14, 43, 44), the maximum level of unsaturation as *S. cerevisiae* are unable to synthesize PUFAs. Deletion of the *TAZI* gene results in increased MLCL, reduced CL and more saturated CL species (45–47). Cells lacking Cldlp also lack remodeled CL but exhibit a milder reduction in its abundance and increased saturation. They have thus been used as a system to investigate the contributions of unremodeled CL to mitochondrial function independent of MLCL (42, 47). Previous reports have shown that *taz1Δ*, but not *cld1Δ*, cells display temperature-sensitive respiratory growth phenotypes (45, 48–50), increased oxidative stress (51), and defective bioenergetic coupling (52). These phenotypes are less severe than those occurring from the complete loss of CL in *crd1Δ* (53). Despite these observations, it has been surprising that these mutants

do not possess altered mitochondrial morphology or ultrastructure (47). The combined *cld1Δtaz1Δ* strain contains an identical PL profile to *cld1Δ*, extinguishes the MLCL:CL ratio, and has been shown to rescue respiratory defects in *taz1Δ* (47, 49, 54).

CL is just one of the several bulk PLs in the IMM, and its functional roles could be dependent on its local lipid environment. In a previous study, we demonstrated that CL synthesis was essential for the formation of highly curved cristae in the IMM under conditions of increased lipid saturation induced by genetic or environmental repression of the acyl-CoA desaturase OleIp (55). Oxygen is a substrate of the OleIp reaction and is bound to the desaturase through a weak, di-iron binding site (56, 57); microaerobic growth thus acts as a natural modulator of lipid saturation. Saturation modulates the extent of ATP synthase oligomerization at cristae ridges, which CL mechanically buffers against (55).

Here, we report phenotypes for loss of CL remodeling in yeast cells with saturated lipidomes. We show that microaerobic growth causes CL remodeling mutants to show a characteristic loss of cristae membranes in yeast mitochondria, which were previously only observed in mammalian models of BTHS. We observe a stronger dependence of IMM ultrastructure on Cldlp activity compared to Tazlp, suggesting that accumulation of unremodeled CL is more deleterious than that of MLCL for the structure of the yeast IMM in these conditions. In mammalian cells, we show that iPLA<sub>2</sub> inhibition only results in mitochondrial abnormalities when cotreated with the saturated fatty acid palmitic acid (Palm). We find that mitochondrial defects in *cld1Δ* yeast cells correspond to a loss of total CL and are partially rescued by deletion of the gene encoding for the mitochondrial phospholipase Dd1lp, which has wide-ranging effects on the composition of CL and its anionic PL precursors.

## MATERIALS AND METHODS

### Yeast strains and growth conditions

All *S. cerevisiae* strains used in this study are described in [supplemental Table S1](#). For aerobic experiments, cells were grown in complete supplement mixture (CSM) (0.5% ammonium sulfate, 0.17% yeast nitrogen base without amino acids, and 2% glucose) medium lacking appropriate amino acids for selection. Yeast mutants were generated by PCR-based homologous recombination, open reading frames (ORF) were replaced by either KanMX (*TAZI*, *DDL1*), *TRP1* (*CLD1*), or *HIS3* (*ATG32*), except for *ddl1Δtaz1Δ* which was generated by replacing the *DDL1* ORF with KanMX and the *TAZI* ORF with *HIS3*.

For aerobic growth conditions, cells were grown overnight in a controlled temperature shaker (200 rpm) at 30°C in CSM synthetic medium containing 2% glucose using 14 ml culture tubes (18 mm diameter) with a snap/vent cap (Greiner). Cells were then backdiluted into 5 ml fresh CSM and then grown until stationary phase prior to analysis. For microaerobic growth, cells were first preincubated in CSM containing 2%

glucose in a controlled temperature shaker overnight at 30°C. Aerobic overnight cultures were then backdiluted 1:25 into 24 ml fresh CSM media (25 ml total volume) in 27 ml elongated glass culture tubes (Pyrex) and subsequently fitted with 15 mm diameter rubber stopper caps with holes, which were connected via tubing to a water source to allow gas outflow while limiting inflow. The tubes were placed in a 30°C incubator (without shaking) and grown for 48 h. After growth, cells reached an OD<sub>600</sub> of ~0.8–1.0. O<sub>2</sub> concentration in microaerobic chambers was estimated to be ~0.2–0.8% of saturation, as measured with a Clarke electrode. Subsequent live cell imaging was conducted on aliquots, and cells were lysed, and flash frozen for lipidomic analysis.

### Mammalian cell culture

HEK293 cells (Sigma-Aldrich) were cultured in DMEM (Gibco) supplemented with 10% fetal bovine serum (FBS, Gibco) in 37°C incubators containing 5% CO<sub>2</sub>. For BEL treatment, cells were seeded and grown for 48 h in 2.5 μM BEL (Cayman Chemical), 100 μM Palm or both, prior to analysis. Palm and OA were prepared as previously described (58): Sodium palmitate or sodium oleate (Thermo Fisher Scientific) was complexed to fatty acid-free bovine serum albumin (BSA, Roche). Fatty acids were dissolved 1:1 in a mixture of 0.1 mM NaOH in HBSS and ethanol to a concentration of 200 mM, heated to 65°C, and then added to a 4.4% BSA HBSS solution that had been heated to 37°C such that the final fatty acid concentration was 2 mM in a 3:1 M ratio with BSA. The mixture was then stirred vigorously and incubated at 37°C for 1 h. The Palm:BSA mixture or 4.4% BSA vehicular control was diluted into complete DMEM containing 10% FBS to a concentration of 100 μM and filtered through a 2 μm polyethersulfone filter (Thermo Fisher Scientific) before use. Cells were seeded and then grown with complete DMEM containing Palm complexed to BSA and subjected to analysis after 48 h. The treatment time was selected as there are no observable defects to organelle morphology, but an increase in esterified saturated fatty acids (58). Cells were routinely tested for mycoplasma.

### Confocal microscopy

Live cell microscopy was conducted using Plan-Apochromat 63x/1.4 Oil DIC M27 objective on the Zeiss LSM 880 with an Airyscan detector; image acquisition and processing was performed with ZEN software ([zeiss.com/microscopy/us/products/software/zeiss-zen.html](http://zeiss.com/microscopy/us/products/software/zeiss-zen.html)) using default processing settings. To assess mitochondrial morphology in yeast grown in either aerobic or microaerobic conditions, strains were transformed with IMM-localized Cox4-GFP, and cells were subsequently grown in CSM containing 2% glucose aerobically overnight prior to backdilution into fresh media and incubation in aerobic or microaerobic growth conditions. After 24 h (aerobic) or 48 h (microaerobic) of incubation, cells were imaged in 8-well coverglass-bottom chambers (Nunc Lab-Tek) pretreated with concanavalin A (Sigma-Aldrich). Cells were imaged using a 488 nm laser line. N > 50 cells in biological triplicates from each condition were then grouped into either normal, encompassing interconnected morphologies, or abnormal, consisting of fragmented and completely ablated mitochondrial structures, as has been previously described (55).

For analysis of mitochondrial membrane potential in yeast strains, aliquots of aerobic or microaerobic cells were incubated with 200 nM of membrane potential sensitive dye

tetramethylrhodamine ethyl ester (Thermo Fisher Scientific T669). Cells were first incubated in the dark with dye for 20 min at room temperature followed by three washes in water prior to imaging with a 561 nm laser line at 0.2% laser power. Relative levels of tetramethylrhodamine ethyl ester fluorescence were quantified in the midplane of N = 20 cells in each condition using ImageJ ([imagej.net/software/fiji/](http://imagej.net/software/fiji/)). Analysis of mitochondrial nucleoids was performed by staining cells with SYBR Green I (SGI, Thermo Fisher Scientific S7563). Cells were first washed with PBS prior to staining with SGI (1:10,000) for 10 min at room temperature in the dark. After staining, cells were washed 3 times with PBS prior to imaging using a 488 nm laser line at 0.1% laser power. The number of nucleoids per cell were quantified in N > 50 cells. Relative levels of reactive oxygen species (ROS) were determined in each strain in aerobic or microaerobic conditions by staining with 20 μM of ROS-sensitive dye (H<sub>2</sub>DCFDA, Thermo Fisher Scientific) for 30 min covered from light. Cells were then washed 3 times with PBS prior to imaging using a 488 nm laser line at 1% laser power. 2',7'-dichlorofluorescein intensity was quantified from N = 20 cells in each condition. For each image, a subsequent differential interference contrast image was taken to ensure that dead cells were not included in the quantification. For staining of vacuole membranes, cells were grown in either CSM containing 2% glucose until stationary phase (aerobic), for 48 h (microaerobic) or for 72 h in CSM containing 3% glycerol. Cells were then stained with 10 μM FM4-64 (Med-ChemExpress) for 30 min in a 30°C shaker in the dark prior to washing once with medium. Cells were then resuspended in fresh media and incubated in a 30°C shaker in the dark for 90 min. After incubation, cells were washed twice with media prior to imaging using a 561 nm laser line at 1% laser power.

For HEK293 samples, cells were first seeded into individual 35 mm Mattek dishes and subjected to treatment with either 100 μM Palm, 2.5 μM BEL or a combination of both, for 48 h prior to staining with 200 nM Mitotracker Deep Red (Thermo Fisher Scientific) for 30 min. Cells were then washed three times with HBSS, resuspended in clear DMEM containing 10% FBS without phenol red, and imaged using a 633 nm excitation at 0.2% laser power.

### Lipidomics analysis

Mass spectrometry-based lipid analysis was performed by Lipotype GmbH as previously described (59, 60). Lipids were extracted using a chloroform/methanol procedure (61). Samples were spiked with internal lipid standard mixture containing: cardiolipin 14:0/14:0/14:0/14:0 (CL), ceramide 18:1/2/17:0 (Cer), diacylglycerol 17:0/17:0 (DAG), lysophosphatidate 17:0 (LPA), lysophosphatidyl-choline 12:0 (LPC), lysophosphatidylethanolamine 17:1 (LPE), lysophosphatidylinositol 17:1 (LPI), lysophosphatidylserine 17:1 (LPS), phosphatidate 17:0/14:1 (PA), phosphatidylcholine 17:0/14:1 (PC), phosphatidylethanolamine 17:0/14:1 (PE), phosphatidylglycerol 17:0/14:1 (PG), phosphatidylinositol 17:0/14:1 (PI), phosphatidylserine 17:0/14:1 (PS), ergosterol ester 13:0 (EE), triacylglycerol 17:0/17:0/17:0 (TAG). After extraction, the organic phase was transferred to an infusion plate and dried in a speed vacuum concentrator. The dry extract was resuspended in 7.5 mM ammonium formate in chloroform/methanol/propanol (1:2:4, V:V:V). All liquid handling steps were performed using Hamilton Robotics STARlet robotic platform with the Anti Droplet Control feature for organic solvents pipetting.

Samples were analyzed by direct infusion on a QExactive mass spectrometer (Thermo Fisher Scientific) equipped with a TriVersa NanoMate ion source (Advion Biosciences). Samples were analyzed in both positive and negative ion modes with a resolution of  $R_{m/z = 200} = 280,000$  for MS and  $R_{m/z = 200} = 17,500$  for MSMS experiments, in a single acquisition. MSMS was triggered by an inclusion list encompassing corresponding MS mass ranges scanned in 1 Da increments (62). Both MS and MSMS data were combined to monitor EE, DAG, and TAG ions as ammonium adducts; lysophosphatidyl-choline and PC as an formiate adduct; and CL, lysophosphatidylserine, PA, PE, PG, phosphatidylinositol, and PS as deprotonated anions. MS only was used to monitor lysophosphatidate, lysophosphatidylethanolamine, and lysophosphatidylinositol as deprotonated anions; Cer as formate adduct.

Data were analyzed with in-house developed lipid identification software based on LipidXplorer ([lifs-tools.org/lipidexplorer](https://lifs-tools.org/lipidexplorer)) (63, 64). Data post processing and normalization were performed using an in-house developed data management system. Only lipid identifications with a signal-to-noise ratio >5, and a signal intensity 5-fold higher than in corresponding blank samples were considered for further data analysis.

### Respirometry

For analysis of respiration in HEK293 cells, cells were treated for 48 h prior to analysis on the Agilent Seahorse XF pro (Agilent Technologies). Subsequently, 15000 cells were seeded in biological replicates ( $n = 4$ ) into 96 well Seahorse cell culture microplates (Agilent Technologies) pretreated with fibronectin (5  $\mu\text{g/ml}$ ). Samples were analyzed using the Seahorse Cell Mito Stress Test, with sequential addition of oligomycin (1.5  $\mu\text{M}$ ), carbonyl cyanide-p-trifluoromethoxy phenylhydrazone (1  $\mu\text{M}$ ) and a Rotenone/Antimycin A mixture (0.5  $\mu\text{M}$ ). Analysis was performed on respiration rates after treatments with inhibitors to readout basal, ATP-linked, maximal and proton leak respiration rates. After the assay, cells were trypsinized and mixed with trypan blue and cell-counted to normalize respiration rates.

### Electron microscopy

After growth in CSM with 2% glucose, aerobic or microaerobic yeast cells were filtered and fixed in a 3% glutaraldehyde solution for 1 h at room temperature and then at 4 °C overnight. Fixed samples were then treated with 0.25 mg/ml zymolyase 20T for 1 h at room temperature prior to washing twice with 0.1 M sodium cacodylate buffer. Samples were then embedded prior to imaging using a JEOL 1400 transmission electron microscope. HEK293 cells were first cultured to confluency in each treatment condition prior to fixation in prewarmed 4% glutaraldehyde solution for 30 min at room temperature. Samples were then refixed and embedded prior to imaging using a JEOL 1400 transmission electron microscope.

ImageJ software was utilized to measure cristae tubule lengths and outer mitochondrial membrane areas from thin section images. For morphological quantification,  $N = 40$  mitochondria were counted in each condition and assigned either tubular, shortened, or flat/empty structural features. Flat/empty structures included mitochondria bereft of cristae as well as those with IMM structures that were adjacent to the outer mitochondrial membrane. Cristae lengths were determined from  $N = 30$  mitochondria in each condition. For

analysis of cristae density in HEK293 cells,  $N = 30$  mitochondria were analyzed.

## RESULTS

### Microaerobic growth conditions promote IMM biogenesis and saturated lipidomes

Native yeast environments, like rotting fruit or fermentation vessels, feature lower oxygen levels compared to those often utilized in laboratory studies. In mammalian cells, reduction of oxygen results in hypoxic stress that renders a loss to mitochondrial morphology (65). We were thus surprised to observe that yeast grown in microaerobic conditions featured mitochondria with elongated cristae, in contrast to shorter structures commonly seen in aerobically grown cells (Fig. 1A). These elongated cristae are more likely to be sheet-like, with greater resemblance to mammalian mitochondria (Fig. 1B), while shorter cristae in aerobic cells likely correspond to tubular structures as has been previously described (67). Cristae elongation could be ascribed to increased expression of genes involved in mitochondrial biogenesis and ETC complexes, but analysis of RNA-seq data previously acquired (66) showed decreased expression of all major ETC components and ATP synthase subunits under microaerobic conditions (Fig. 1C). Instead, increases in expression were observed for the CL remodeling genes, *CLD1* and *TAZI*, suggesting a heightened role for this pathway under low oxygen (Fig. 1C). Changes in expression of CL remodeling enzymes was not observed for CL synthase itself (*CRDI*) and were exclusive to cells subjected to extended long-term microaerobic growth, rather than short-term hypoxia (supplemental Fig. S1A). These observations suggested that CL remodeling could respond to changes in mitochondrial lipids during long-term low oxygen exposure, a hallmark of natural yeast fermentation.

Growth in low oxygen has been shown to increase the presence of saturated fatty acids through inhibition of fatty acid desaturases (68, 69). In yeast, a reduction in oxygen inhibits the activity of the sole lipid desaturase, *Ole1p* (56, 57). As a result, microaerobic yeast cells have reduced levels of unsaturated PLs with 1 or 2 double bonds (DB) and increased levels of fully saturated PLs with 0 DB (Fig. 1D). Elevated levels of saturated lipids have been associated with the induction of ER stress responses in mammalian cells, such as the unfolded protein response. However, we observed no elevated unfolded protein response activation or changes to ER morphology under microaerobic conditions (supplemental Fig. S1B, C), suggesting that they do not represent a condition of fatty acid stress. Indeed, for highly abundant PLs like PC or PE, microaerobic yeast lipidomes better mimic the acyl chain profile of mammalian cells with saturated *sn-1* and unsaturated *sn-2* chains (supplemental Fig. S2), in contrast to diunsaturated PLs in yeast grown under high aeration (55). In CL, we observed a major change in the

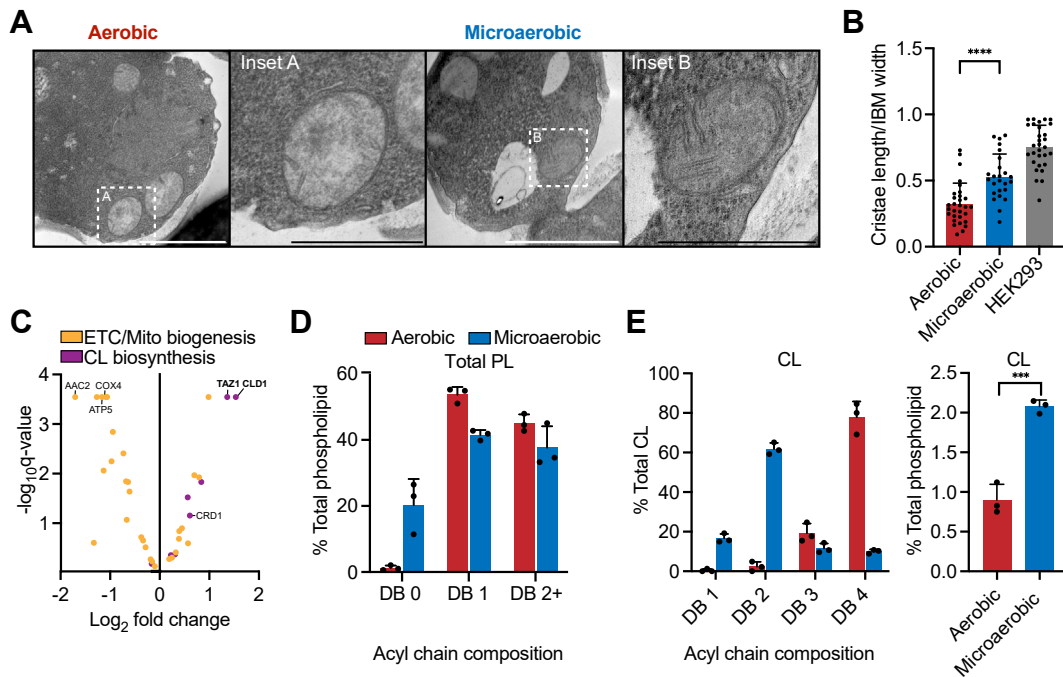


**Fig. 1.** Microaerobic yeast feature elongated cristae structures and are enriched in CL. **A:** Thin-section TEM images of mitochondria from yeast grown in glucose medium under aerobic and microaerobic conditions. Scale bars, 1000 nm. Insets scale bar, 500 nm. **B:** Microaerobic cells have increased cristae length, more resembling those of the mammalian cell line HEK293. Cristae lengths were quantified relative to the width of the inner boundary membrane from  $N = 30$  mitochondria per condition.  $****P < 0.0001$  unpaired  $t$  test of aerobic versus microaerobic yeast. Error bars indicate SD. **C:** Gene expression changes in cells under microaerobic versus aerobic growth implicates an increase in CL remodeling, but not CL biosynthesis. Reduced expression was observed for ETC components and proteins involved in mitochondrial biogenesis. RNA-seq data were originally collected and described in (66), data are available at the gene expression omnibus (accession number: GSE94345). **D:** Microaerobic yeast cells possess more saturated PLs (DB 0) compared to aerobic cells as determined from lipidomic analysis on whole cells ( $n = 3$ ). Error bars indicate SD. **E:** *Left:* Microaerobic yeast cells contain higher CL saturation (DB 1 and DB 2), but also an increase in total CL abundance (right). Relative levels of CL were determined by lipidomics ( $n = 3$ ).  $***P = 0.0007$  unpaired  $t$  test of aerobic versus microaerobic cells. CL, cardiolipin; ETC, electron transport chain; PL, phospholipid; TEM, transmission electron microscopy.

unsaturation profile from predominantly 4 DB in aerobic conditions to 2 DB in microaerobic conditions (Fig. 1E). This change was coupled with a 2-fold increase in total CL abundance. Thus, microaerobic growth is characterized by a proliferation in mitochondrial cristae alongside an accumulation of saturated CL, potentially necessitating elevated activity of the remodeling pathway.

### Requirements for CL remodeling under microaerobic conditions driven by lipid saturation

We first asked if the increased levels of lipid saturation under microaerobic growth may provide an elevated role for CL remodeling in maintaining mitochondrial structure, as hinted by the increased expression of *CLD1* and *TAZI* under these conditions (Fig. 1C). In microaerobic conditions, we observed aberrant mitochondrial morphologies and reduced outgrowth in glucose for remodeling mutants, particularly in *cll1Δ* and *cll1Δtaz1Δ*, that were not present under aerobic growth (Fig. 2A–C). TEM analysis also revealed shortened cristae tubules for *taz1Δ* and a complete absence of cristae structures in *cll1Δ* and *cll1Δtaz1Δ* cells in microaerobic conditions (Fig. 2D).

These cells instead featured flat IMM that we previously observed in *crd1Δ* yeast, which lack CL, grown under microaerobic conditions or in backgrounds where lipid saturation was increased genetically (55). The effect of microaerobic growth on mitochondrial morphology was rescued by medium supplementation with OA (supplemental Fig. S3A–C). Exogenous supplementation of Palm, but not OA, resulted in abnormal mitochondrial morphology in aerobic cultures bereft of CL remodeling (supplemental Fig. S3D), indicating that CL remodeling phenotypes under microaerobic conditions were the direct result of lipid saturation.

Significant defects in cristae architecture are often interlinked with respiratory dysfunction in mitochondria. Since direct measurement of cellular respiration in microaerobic conditions is challenging, we instead tested other proxies of yeast mitochondrial function: outgrowth on nonfermentable carbon sources (ethanol/glycerol), membrane potential, reactive oxygen species (ROS), and mitochondrial DNA (mtDNA) nucleoid formation. While no changes to growth on ethanol/glycerol were observed in remodeling mutants in aerobic growth conditions, *cll1Δ* and *cll1Δtaz1Δ* were

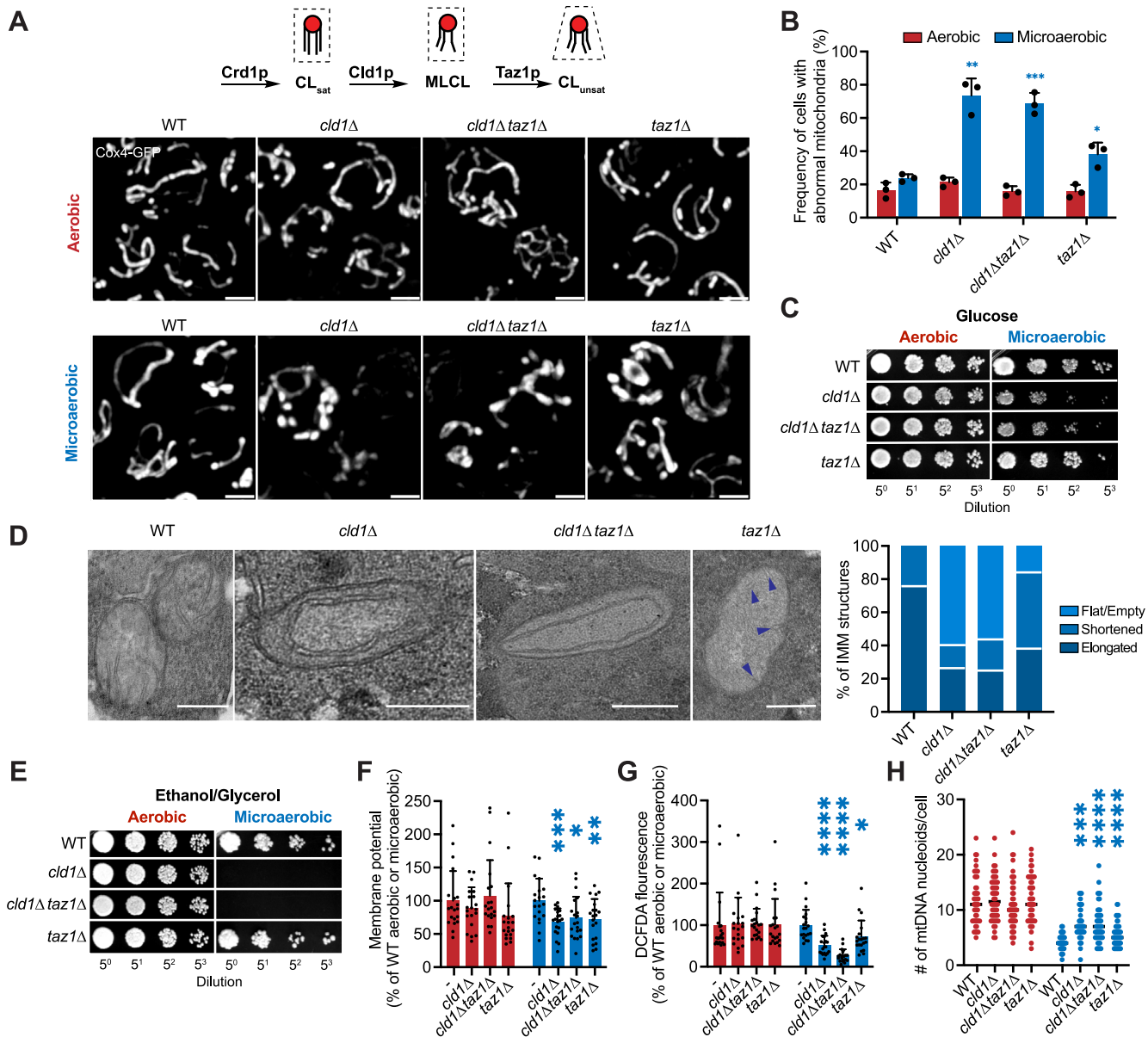


**Fig. 2.** Loss of CL remodeling enzymes in microaerobic conditions results in altered IMM structure and mitochondrial dysfunction. **A:** In aerobic conditions, loss of CL remodeling enzymes does not result in changes to mitochondrial morphology. However, in microaerobic conditions, *cld1Δ*, *cld1Δtaz1Δ*, and *taz1Δ* cells show fragmented and swollen mitochondria. The 3D projections of yeast cells expressing IMM-localized Cox4-GFP are shown. Scale bars, 2  $\mu$ m. **B:** Quantification of differences in the relative amounts of abnormal mitochondria in yeast strains bereft of CL remodeling enzymes grown in either aerobic or microaerobic conditions.  $N > 50$  cells were scored in each biological replicate. \* $P < 0.05$ , \*\* $P < 0.005$ , \*\*\* $P < 0.001$  from unpaired *t*-tests against microaerobic WT and error bars indicate SD ( $n = 3$ ). **C:** Loss of CL remodeling results in reduced fitness under microaerobic conditions. Liquid cultures were grown in aerobic (*left*) or microaerobic (*right*) conditions prior to serial dilution onto YPD agar plates, which were incubated under standard conditions. **D:** CL remodeling mutants exhibit altered ultrastructure of cristae under microaerobic conditions. *Left* thin section TEM of *cld1Δ* and *cld1Δtaz1Δ* microaerobic cells showed mitochondria with long, circular IMM structures that spanned the length of the outer mitochondrial membrane and resemble flat cristae structures. Mitochondria from *taz1Δ* cells showed shortened cristae tubules (marked with *arrows*). WT cells possessed mitochondria with elongated (>200 nm) cristae sheets, as shown in [Figure 1](#). Scale bars, 250 nm. *Right* types of cristae/IMM observed by TEM were quantified from  $N > 40$  mitochondria in each condition. **E:** Microaerobic cells lacking Cld1p are unable to grow on nonfermentable carbon sources. Liquid cultures in glucose medium were grown in either aerobic (*left*) or microaerobic conditions (*right*) prior to serial dilutions on YPEG agar plates, which were incubated under standard conditions. Only cells with functional mitochondria can form colonies on ethanol/glycerol as a carbon source in YPEG. **F:** Mitochondrial potential was assayed under aerobic or microaerobic conditions. Maximum intensity of mitochondria in cells stained with 200 nM TMRE was measured using line profile analysis at the midplane of each cell,  $N = 20$  per condition. \*\*\* $P = 0.0008$ , \* $P = 0.0162$ , and \*\* $P = 0.0091$  and unpaired *t* test for *cld1Δ*, *cld1Δtaz1Δ*, and *taz1Δ*, respectively against WT. **G:** Loss of CL remodeling dampens ROS levels under microaerobic conditions. ROS was assayed by microscopy after incubation of aerobic or microaerobic cells with 20  $\mu$ M H<sub>2</sub>DCFDA dye. Intensity was determined using line profile analysis at the midplane of each cell.  $N = 20$  cells were analyzed per condition. \* $P = 0.0249$ , \*\*\* $P < 0.0001$  unpaired *t* test of *taz1Δ*, *cld1Δ*, and *cld1Δtaz1Δ*, respectively against WT. **H:** Cells containing unremodeled CL exhibit increased numbers of mtDNA nucleoids compared to WT under

unable to grow after preculture in microaerobic conditions, indicating significant mitochondrial dysfunction (Fig. 2E). In all CL remodeling mutants, we also observed decreases in membrane potential (Fig. 2F), ROS levels (Fig. 2G), and the number of mtDNA nucleoids (Fig. 2H) due to their clustering as has been described previously (55, 70, 71) (Fig. 2E and supplemental Fig. S4), all which imply mitochondrial defects. Akin to our examination of cristae structure, mitochondrial dysfunction was heightened in *cll1Δ* and *cll1Δtaz1Δ* backgrounds compared to *taz1Δ*, implying a greater role for loss of CL remodeling than accumulation of MLCL under microaerobic conditions.

### BTHS mutations drive mitochondrial abnormalities under microaerobic conditions

We next asked whether specific patient-derived BTHS mutants in tafazzin could drive changes in mitochondrial morphology. While mitochondrial defects in *taz1Δ* were lower than those of *cll1Δ* and *cll1Δtaz1Δ* under microaerobic conditions, *taz1Δ* cells still exhibited significant perturbations compared to WT (Fig. 2B, F–H). To test whether specific BTHS mutations accrued a similar effect on the mitochondria in these conditions, we used a previously described set of yeast strains that express *TAZI* harboring mutations in conserved regions of human TAZ that also occur in BTHS (34, 46). These two BTHS-associated mutations, A88R and G230R, occur in the conserved acyltransferase domain and the membrane anchor region respectively. A88R and G230R feature defective Tazlp higher-order organization, causing cells to exhibit increases in MLCL and reductions in CL (34). Under aerobic conditions, BTHS mutants did not elicit alterations to mitochondrial morphology, function, or ultrastructure (Fig. 3A–D). However, under microaerobic growth, both mutants displayed altered IMM morphology, reduced potential, and a loss of cristae ultrastructure (Fig. 3A–D). These results demonstrate that BTHS-associated mutations can drive alterations to the yeast IMM when cells are grown under reduced oxygenation.

### Interactions between CL remodeling and lipid saturation are extendable to mammalian cells

With the strong interaction between Cldlp loss and microaerobic yeast growth, we asked whether inhibition of CL remodeling leads to loss of IMM ultrastructure in other cell types exposed to elevated lipid saturation. While no homolog of Cldlp exists in mammalian cells, the iPLA<sub>2</sub> family of enzymes conducts an identical deacylation reaction on CL (21). We hypothesized that iPLA<sub>2</sub> inhibition would elicit a

similar sensitivity of mitochondrial structure to lipid saturation as we had observed in yeast. To test this, we treated HEK293 cells with the iPLA<sub>2</sub> inhibitor BEL, which has been shown previously to prevent MLCL formation by instead increasing the levels of nascent, unremodeled CL (22). To induce changes in lipid saturation, we fed cells with the saturated fatty acid Palm complexed to BSA at 100 μM, a concentration that does not induce any independent changes to mitochondrial functions (58, 72). We observed that BEL + Palm-treated cells exhibited respiratory dysfunction as well as perturbed mitochondrial morphology and ultrastructure (Fig. 4A–C), which was not displayed in independent treatments of each compound or upon treatment with unsaturated OA (supplemental Fig. S3E–G). These results corroborate our findings in yeast and suggest that the inhibition of CL remodeling deacylation may be particularly sensitive to environmental saturated lipid levels.

### Remodeling is coupled to total CL levels in microaerobic conditions

We next sought to delineate the lipidic drivers that led to mitochondrial dysfunction in yeast CL remodeling mutants under microaerobic, but not aerobic, growth conditions. Under aerobic conditions, we observed a ~50% reduction in CL levels in each of the CL remodeling mutants compared to WT, and no changes to the CL precursor PG (Fig. 5A). Contrastingly, under microaerobic conditions, no CL was detected in *cll1Δ* or *cll1Δtaz1Δ* mutants and a ~75% reduction in CL was observed in *taz1Δ* (Fig. 5B). This loss in CL levels was coupled with increased PG, which suggested an inhibition of CL synthase. However, abrogation of CL synthesis in *crd1Δ* cells under microaerobic conditions produced much greater levels of PG, to ~3% of all PLs (55), suggesting that inhibition of Crdlp is not the only factor contributing to loss of CL in *cll1Δ* or *cll1Δtaz1Δ*. We note that our analysis did not include quantification of MLCL, so we preclude that changes in its levels also occur under microaerobic growth.

Further analysis of acyl chain composition revealed changes in CL resulting from the interplay of remodeling and saturation. Under aerobic conditions, *cll1Δ* and *cll1Δtaz1Δ* accumulate CL containing 3 DB instead of 4 DB; *taz1Δ* also accumulated 3 DB CL as the principal species but also contained more saturated CL with low levels of 2 or 1 DB (Fig. 5C). Thus, all remodeling mutants under aerobic growth retain a highly unsaturated CL (3 DB) as the predominant species. In contrast, microaerobic growth altered the CL saturation levels from 4 DB to 2 DB in WT cells, while the most abundant CL molecule in microaerobic *taz1Δ* was

---

microaerobic conditions. To image mtDNA nucleoids, cells were stained with SYBR Green I (SGI). The number of individual nucleoids in each cell were quantified using imageJ software, N = 50 per condition. \*\*\**P* = 0.0005, \*\*\*\**P* < 0.0001 unpaired *t* test of *cll1Δ*, *taz1Δ* and *cll1Δtaz1Δ* respectively against WT. IMM, inner mitochondrial membrane; CL, cardiolipin; TMRE, tetramethylrhodamine ethyl ester; ROS, reactive oxygen species; YPD, yeast extract peptone dextrose; YPEG, yeast extract peptone ethanol glycerol.



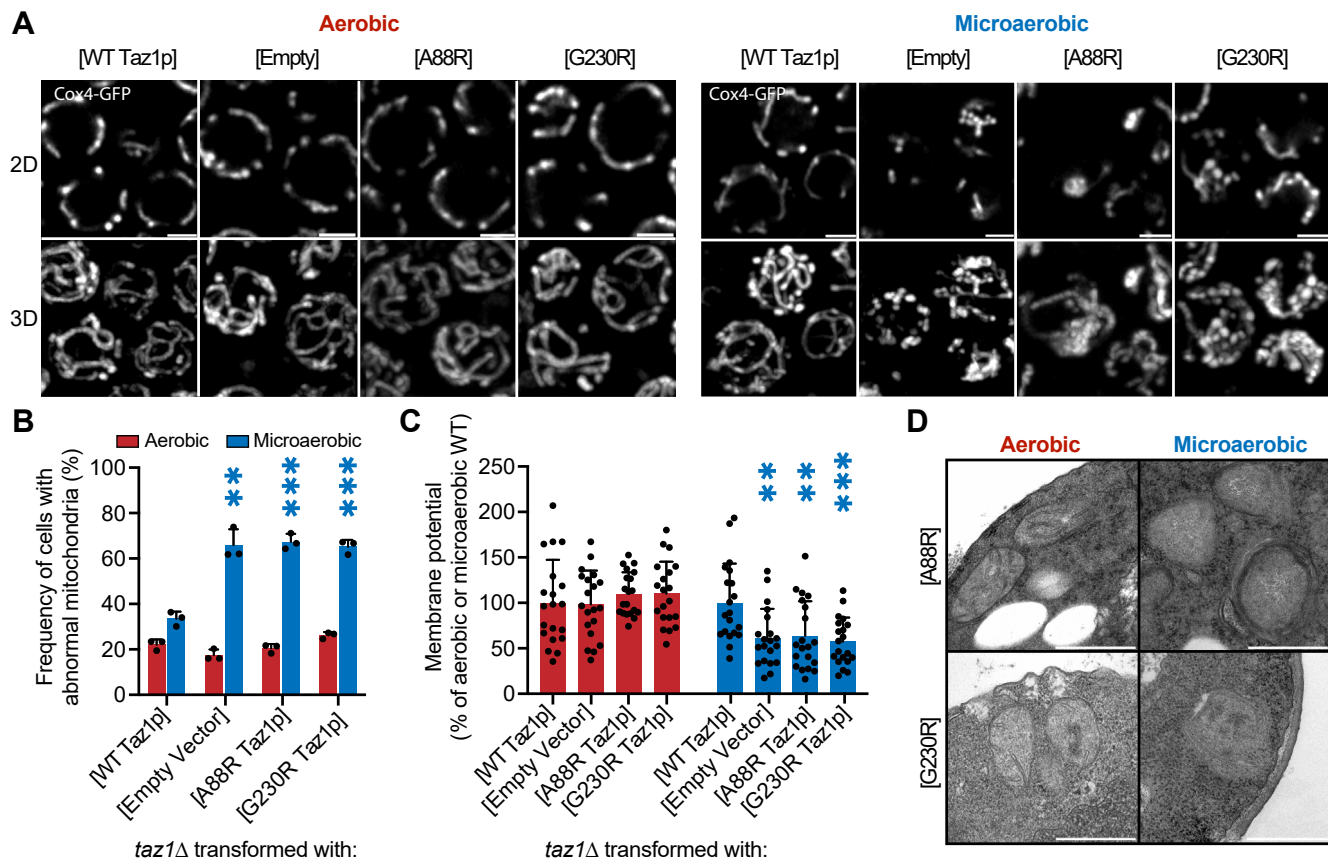


**Fig. 3.** BTHS-associated Taz1p mutations exhibit abnormal mitochondrial architecture under microaerobic conditions. **A:** Cells expressing BTHS mutations in conserved regions of Taz1p (BTHS mutants) show abnormal mitochondrial morphology under microaerobic, but not aerobic, growth conditions. Shown are example images of 2D and 3D projections of cells expressing IMM-localized Cox4-GFP. Scale bars, 2  $\mu$ m. **B:** Quantification of the relative amount of morphological defects in *taz1* $\Delta$  strains rescued with Taz1p harboring BTHS mutants compared to those rescued by WT Taz1p.  $N > 50$  cells were quantified in biological triplicates in either aerobic or microaerobic growth conditions. \*\* $P = 0.0018$  unpaired *t* test of empty vector against WT in microaerobic conditions. \*\*\* $P = 0.0002$  for A88R and G230R Taz1p against WT in microaerobic conditions. Error bars indicate SD. **C:** Microaerobic growth results in reduced membrane potential in BTHS mutants compared to rescue. Cells were stained with 200 nM TMRE prior to imaging. \*\*\* $P = 0.0006$  unpaired *t* test of G230R Taz1p against WT Taz1p under microaerobic conditions. \*\* $P = 0.0027$  and  $0.0078$  unpaired *t* test of WT against empty vector and A88R Taz1p, respectively. **D:** The BTHS rescue mutants, A88R and G230R, exhibit flat and empty inner membranes specifically under microaerobic conditions, while retaining cristae tubules under aerobic growth. Scale bars, 500 nm. IMM, inner mitochondrial membrane; BTHS, Barth syndrome; TMRE, tetramethylrhodamine ethyl ester.

predominantly saturated (1 DB) (Fig. 5D). These results aligned with our previous observations that high levels of genetically induced lipid saturation induced significant mitochondrial defects, increased CL saturation to 1 DB, and drove a 2-fold depletion in CL levels without changing PG abundance or saturation (55). They suggest that a combination of increased CL saturation and reduced abundance could drive mitochondrial abnormalities under microaerobic conditions.

### Interactions between the phospholipase Ddl1p and the remodeling pathway

The loss of CL in *clid1* $\Delta$  backgrounds, but lack of accumulation of PG to *crd1* $\Delta$  levels, suggested that CL could be degraded when the remodeling pathway is absent under microaerobic conditions. We first considered whether mitophagic flux to the vacuole could drive CL degradation, as there is some evidence linking CL composition to mitophagy (73, 74). To test

this, we measured the incorporation of mitochondrial Cox4-GFP intensity within the vacuole. As a comparison, we grew cells in glycerol for 72 h, which induces mitophagy (75), and used a mitophagy-incapable *atg32* $\Delta$  background as a control for the inhibition of mitophagy (76). Under glycerol growth conditions, WT, *clid1* $\Delta$ , and *taz1* $\Delta$  all exhibited Cox4-GFP signal within the vacuole, while Cox4-GFP signal in *atg32* $\Delta$  was at the periphery of the cell and not in the vacuole (supplemental Fig. S5). Neither WT nor CL remodeling mutants exhibited any vacuolar Cox4-GFP signal under microaerobic conditions. Thus, CL loss is unlikely to result from robust mitophagy under these conditions.

An alternative hypothesis is that CL can be specifically cleared through phospholipase activity. In BTHS patient-derived cell lines and *Drosophila*, defects in remodeling are proposed to drive enhanced turnover of CL via degradation from MLCL (77). However, loss of Cld1p, which prevents MLCL production, reduces CL

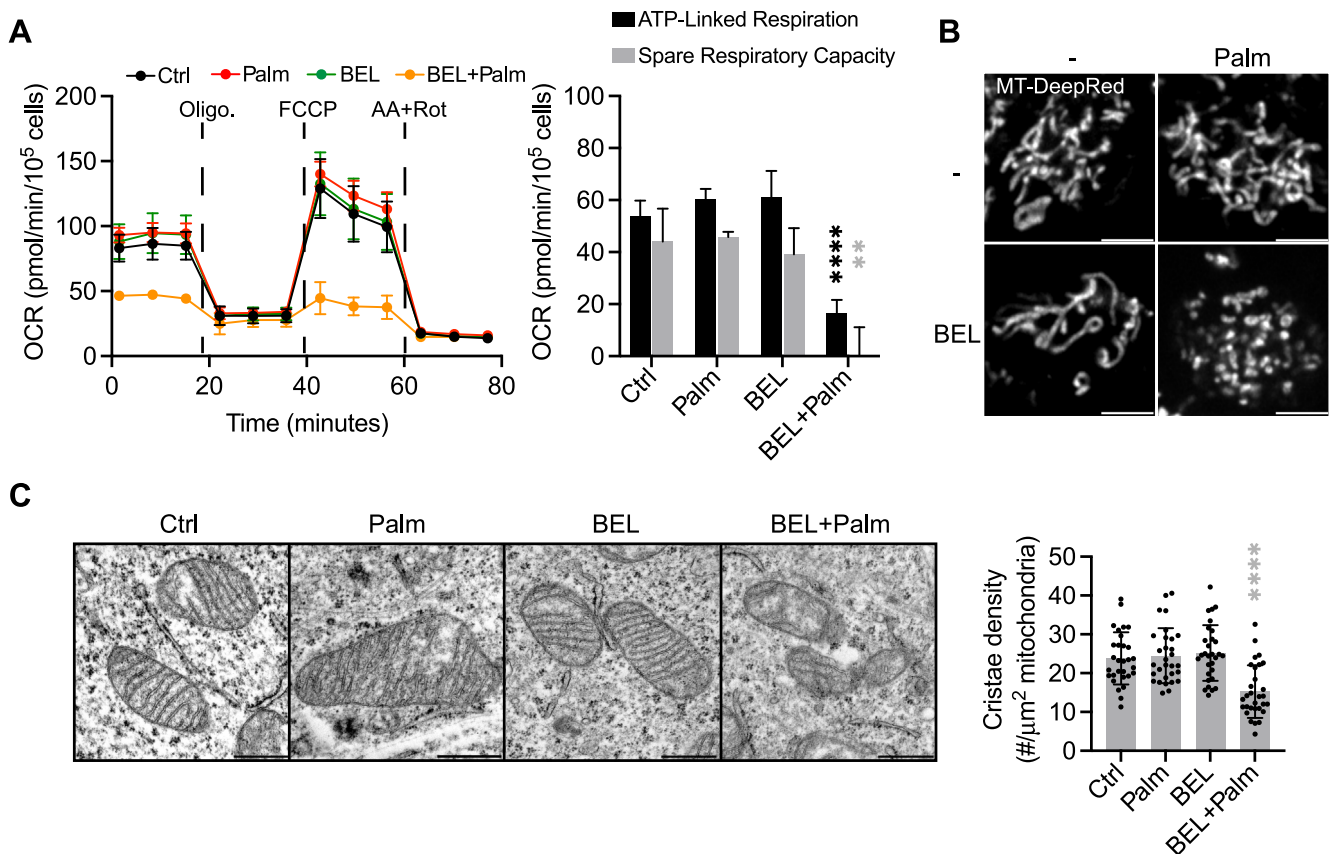


**Fig. 4.** iPLA<sub>2</sub> inhibition in saturated lipid environments results in mitochondrial dysfunction. **A:** Seahorse respirometry of HEK293 cells treated with 2.5 μM bromoenol lactone (BEL) and 100 μM palmitate (Palm) results in reduced cellular respiration and a defective mitochondrial stress response. ATP-linked respiration is calculated from the decrease in oxygen consumption rate upon oligomycin (Oligo.) injection. The spare respiratory capacity is an indicator of the cellular response to increased energetic demand and is defined as the difference between maximal and basal respiration. Defects in ATP-linked respiration and spare respiratory capacity are indicative of general ETC dysfunction in BEL + Palm cells. Wells containing 15,000 cells were treated in biological replicates (n > 3) for 48 h prior to analysis. \*\*\*\*P < 0.0001 and \*\*P = 0.0019 unpaired *t* test of BEL + Palm against Ctrl for ATP-linked respiration and spare respiratory capacity respectively. Error bars indicate SD. **B:** The combined treatment of BEL and Palm (BEL + Palm) results in fragmented mitochondria. HEK293 cells were treated as in (A) for 48 h prior to imaging using 200 nM Mitotracker DeepRed FM. Scale bars, 5 μm. **C: Left** BEL + Palm results in empty mitochondria with few cristae, while all other conditions showed no defects in cristae density. Scale bars, 500 nm. **Right** cristae density was measured for N = 30 mitochondria in each condition. Error bars indicate SD. \*\*\*\*P < 0.0001 unpaired *t* test of BEL + Palm against Ctrl. ETC, electron transport chain; iPLA<sub>2</sub>, phospholipase A<sub>2</sub>; BEL, bromoenol lactone; Palm, palmitate.

levels in yeast, suggesting other mechanisms of breakdown. Apart from Cld1p, only the mitochondrial phospholipase A<sub>1</sub>, Ddl1p, has been implicated with putative CL hydrolase activity in yeast. Ddl1p has activity toward PA, PG, PC, and PE as substrates (78, 79), but has also been shown to act on TOCL and MLCL (79).

We asked if loss of Ddl1p could restore mitochondrial function in remodeling mutants that exhibit reduced CL. Under aerobic conditions, *ddl1Δ* cells exhibited fragmented mitochondrial structures (Fig. 6A), as has been previously described (79). Surprisingly, mitochondrial fragmentation was mitigated in *cld1Δddl1Δ* and *ddl1Δtaz1Δ* cells, suggesting an interaction between Ddl1p and the remodeling pathway. Under microaerobic conditions, *ddl1Δ*, *cld1Δddl1Δ*, and *ddl1Δtaz1Δ* cells all exhibited significantly aberrant IMM morphologies (Fig. 6A). However, short cristae tubules were observed in *cld1Δddl1Δ* under microaerobic conditions,

unlike *cld1Δ* cells that feature a flat IMM (Fig. 6B). In microaerobic conditions, both *ddl1Δ* and *cld1Δddl1Δ* cells exhibited similar cristae structures and average lengths to *taz1Δ* (Fig. 6B, C). When microaerobically grown *cld1Δddl1Δ* cells were spotted on ethanol/glycerol plates, they regained viability that was lost in *cld1Δ* (Fig. 6D). Loss of Ddl1p can therefore partially rescue IMM structure and function in *cld1Δ* backgrounds under microaerobic conditions.

We next conducted lipidomic analysis on aerobic and microaerobic cells of *ddl1Δ* in the presence and absence of CL remodeling mutants (Fig. 7). We focused on the abundances and compositions of the PLs involved in the CL biosynthetic pathway: PA, PG, and CL, all of which have been shown to be substrates for Ddl1p in vitro (Fig. 7A). Under aerobic conditions, removal of *DDL1* in WT and CL remodeling-deficient backgrounds increased CL, but also PA and PG (Fig. 7B). In *cld1Δ* and

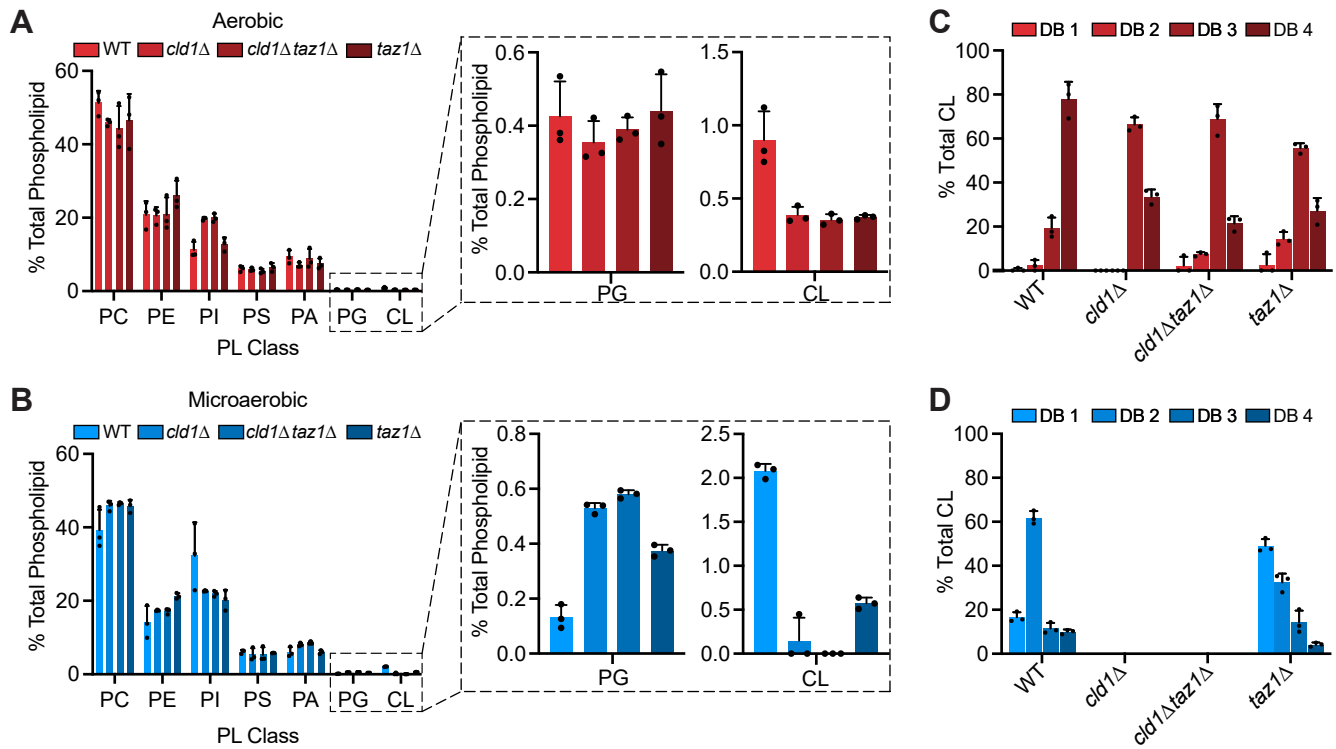


**Fig. 5.** Differential lipidic changes under aerobic and microaerobic conditions in CL remodeling mutants. A: Under aerobic conditions, removal of CL remodeling enzymes results in decreased CL levels without changes to the precursor PG. Error bars indicate SD ( $n = 3$ ). B: Under microaerobic conditions, loss of CL remodeling enzymes results in a significant depletion of CL in *taz1Δ* cells and ablation of CL levels in *cld1Δ* and *cld1Δtaz1Δ* cells. A concomitant increase in PG levels was observed in each mutant, consistent with inhibition of CL synthase. Error bars indicate SD ( $n = 3$ ). C: Aerobic CL remodeling mutants exhibit a shift in the CL profile from 4 DB to 3 DB. Error bars indicate SD ( $n = 3$ ). D: Microaerobic cells have more saturated CL molecules (4 DB to 2 DB), and removal of Taz1p shifts the saturation level of CL to predominantly 1 DB. No data are shown for *cld1Δ* and *cld1Δtaz1Δ* samples, as these predominantly had no detectable CL. Error bars indicate SD ( $n = 3$ ). CL, cardiolipin; PG, phosphatidylglycerol.

*taz1Δ* backgrounds, deletion of *DDL1* returned CL to WT levels, which may explain the rescue of mitochondrial morphology observed under aerobic growth (Fig. 6A). Major increases in PA and PG were observed in *cld1Δddl1Δ* and *ddl1Δtaz1Δ*, but only minor changes in *ddl1Δ* (Fig. 7B), suggesting that the increase in CL synthesis could be driven by increased PA in the absence of CL remodeling. Under microaerobic conditions, Ddl1p-deficient cells showed minimal CL levels in all backgrounds (Fig. 7C). Notably, increased PG was observed in *ddl1Δ* and *taz1Δddl1Δ*, but not in *cld1Δddl1Δ*, suggesting increased flux toward CL synthesis in *cld1Δddl1Δ* without increasing CL levels, indicative of an alternative mechanism of CL loss. Increases in PA, however, were observed in all backgrounds (Fig. 7C). While CL and PG are exclusively localized to mitochondria in yeast, PA is not, and we note that this analysis did not directly measure mitochondrial PA.

In addition to modifying PL biosynthesis, loss of Ddl1p drove differential changes to PL acyl chain composition under aerobic and microaerobic growth. In aerobic conditions, *DDL1* deletion affected the CL chain composition of remodeling mutants. Most notably, a large increase in DB 2 CL was observed in *ddl1Δtaz1Δ* compared to *taz1Δ* cells (Fig. 7D and

supplemental Fig. S6A). There was also a consistent appearance of fully saturated PG in each of the *ddl1Δ* mutants, which were not observed in any of the parental strains (Fig. 7E). Under microaerobic conditions, PG and PA saturation levels also increase in *ddl1Δ* backgrounds (Fig. 7F and supplemental Fig. S6B). Minor changes were observed to CL saturation under microaerobic conditions, but the low overall levels of CL made these difficult to define (supplemental Fig. S6B). Taken together, these data suggest that Ddl1p could modulate CL levels through activity on its precursors PA and PG.

## DISCUSSION

In this study, we address why removal of CL remodeling enzymes do not render any morphological or ultrastructural phenotype in yeast (47). We showed that CL remodeling is essential for mitochondrial structure and function under microaerobic growth conditions, in which the yeast lipidome is defined by increases in lipid saturation. Microaerobically grown remodeling mutants exhibited a loss of highly curved cristae in the IMM, which resemble structures observed in BTHS patients (32) but are not seen in aerobically

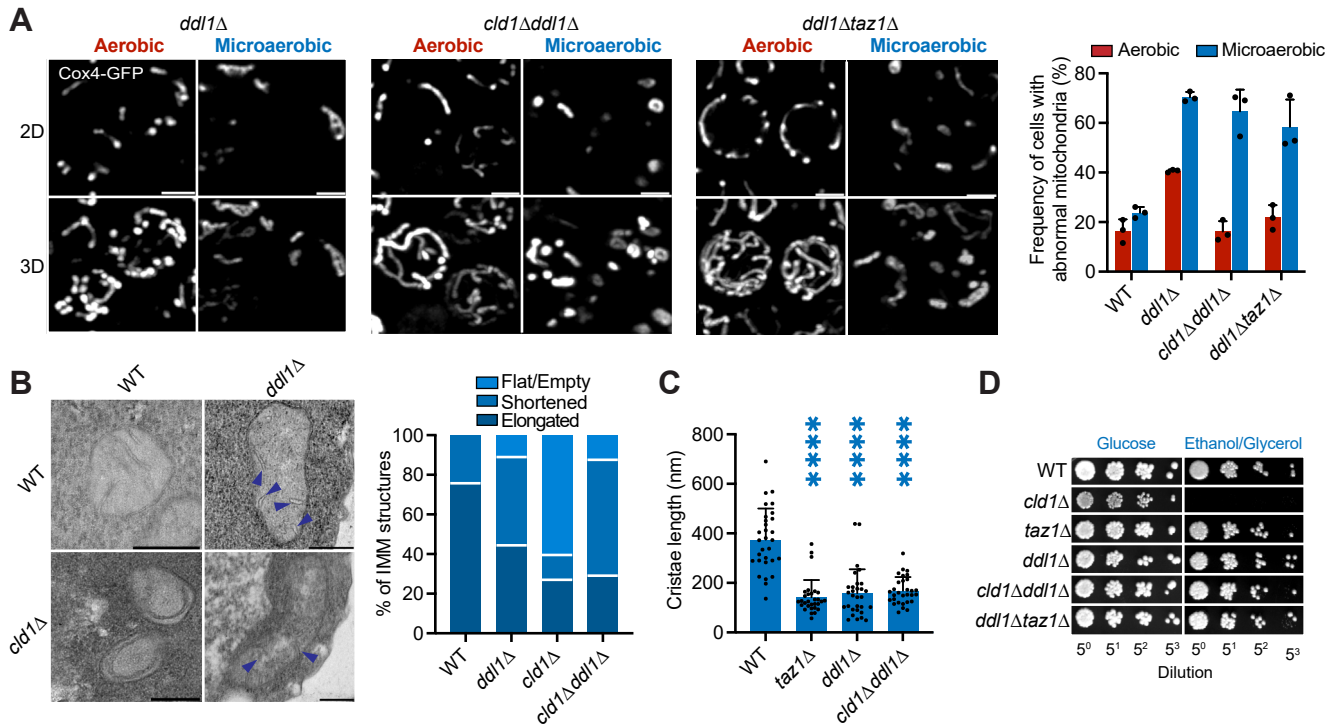


**Fig. 6.** *DDL1* deletion partially rescues cristae structure in *cld1Δ* backgrounds under microaerobic conditions. **A:** Mitochondrial morphologies of *ddl1Δ* cells. Yeast expressing IMM-localized Cox4-GFP were grown in biological replicates ( $n = 3$ ) under aerobic or microaerobic conditions prior to imaging. Scale bars, 2  $\mu\text{m}$ . For analysis of mitochondrial morphology (right),  $N > 50$  cells were quantified in each condition. All *ddl1Δ* strains exhibit elevated abnormal mitochondrial morphology under microaerobic growth, but removal of Cld1p or Taz1p reduces aerobic abnormality in the *ddl1Δ* background.  $**P = 0.0096$  and  $*P = 0.0269$  unpaired *t* test for *cld1Δddl1Δ* and *ddl1Δtaz1Δ* against *ddl1Δ* respectively. Error bars indicate SD. **B:** *ddl1Δ* cells have shortened cristae tubules as determined by thin-section TEM analysis. Arrows indicate shortened cristae tubules. Scale bars, 250 nm. In each condition  $N = 40$  mitochondria were quantified as containing either tubular, shortened, or flat cristae. **C:** *cld1Δddl1Δ* restores cristae tubules lost in microaerobic *cld1Δ* backgrounds, although they are of a shorter length than WT cells. Cristae length was quantified from  $N = 30$  mitochondria from each condition.  $***P < 0.0001$  unpaired *t* test of *taz1Δ*, *ddl1Δ*, and *cld1Δddl1Δ* against WT. **D:** Deletion of *DDL1* in *cld1Δ* backgrounds restores mitochondrial viability after microaerobic growth. Cells were grown in liquid medium under microaerobic conditions for 48 h prior to serial dilution onto either YPD or YPEG plates, which were incubated at standard conditions. IMM, inner mitochondrial membrane; PG, phosphatidylglycerol; TEM, transmission electron microscopy; YPD, yeast extract peptone dextrose; YPEG, yeast extract peptone ethanol glycerol.

grown yeast mutants. *cld1Δ* showed a depletion in CL levels and phenotypes mimicked the severity of microaerobic *crd1Δ* cells that we described previously (55). We extended this observation to mammalian cells, where the abundance of cristae in BEL-treated HEK293 cells was reduced upon a mild treatment of exogenous saturated fatty acids. These data support a model that the role of CL remodeling can be dependent on the overall fatty acid metabolism of cells. They also suggest that the function of the yeast remodeling pathway could be to act during microaerobic growth, a natural condition that promotes lipid saturation.

Yeast cells grown under vigorous laboratory aeration have high levels of unsaturated lipids, which may mask the defects associated with the removal of CL remodeling enzymes. Under aerobic conditions, remodeling mutants retain high levels of CL unsaturation (3 DB) because the substrates for CL synthesis are predominantly di-unsaturated (supplemental Fig. S2). Under microaerobic conditions, CL in *taz1Δ* is predominantly saturated (1 DB) and CL is lost in *cld1Δ* (Fig. 5B, D). These

differences could have significant effects on the properties of CL. While fully unsaturated CL (TOCL) can adopt high-curvature nonlamellar phases (80–82), fully saturated—tetra-palmitic (16:0) or tetra-myristic (14:0)—CL exhibit gel phases (82, 83) that are likely unsuitable for functions in the IMM. The number of saturated acyl chains incorporated in CL could thus drive significant changes in its biophysical properties, which may be crucial for proper cristae assembly. Protein complexes like MICOS and ATP synthase dimers also contribute to IMM curvature (84–86) and their decreased expression during microaerobic conditions might act as an additional factor in increasing the dependence on PL composition for shaping IMM morphology. The predominant unsaturated form of MLCL (47) also adopts lamellar phases, indicating a reduced curvature than remodeled CL (87–89), and fails to interact with ETC complexes and supercomplexes (77).

A general paradigm of BTHS pathophysiology is that MLCL levels are the primary drivers of ETC dysfunction and reduced respiratory capacity observed in

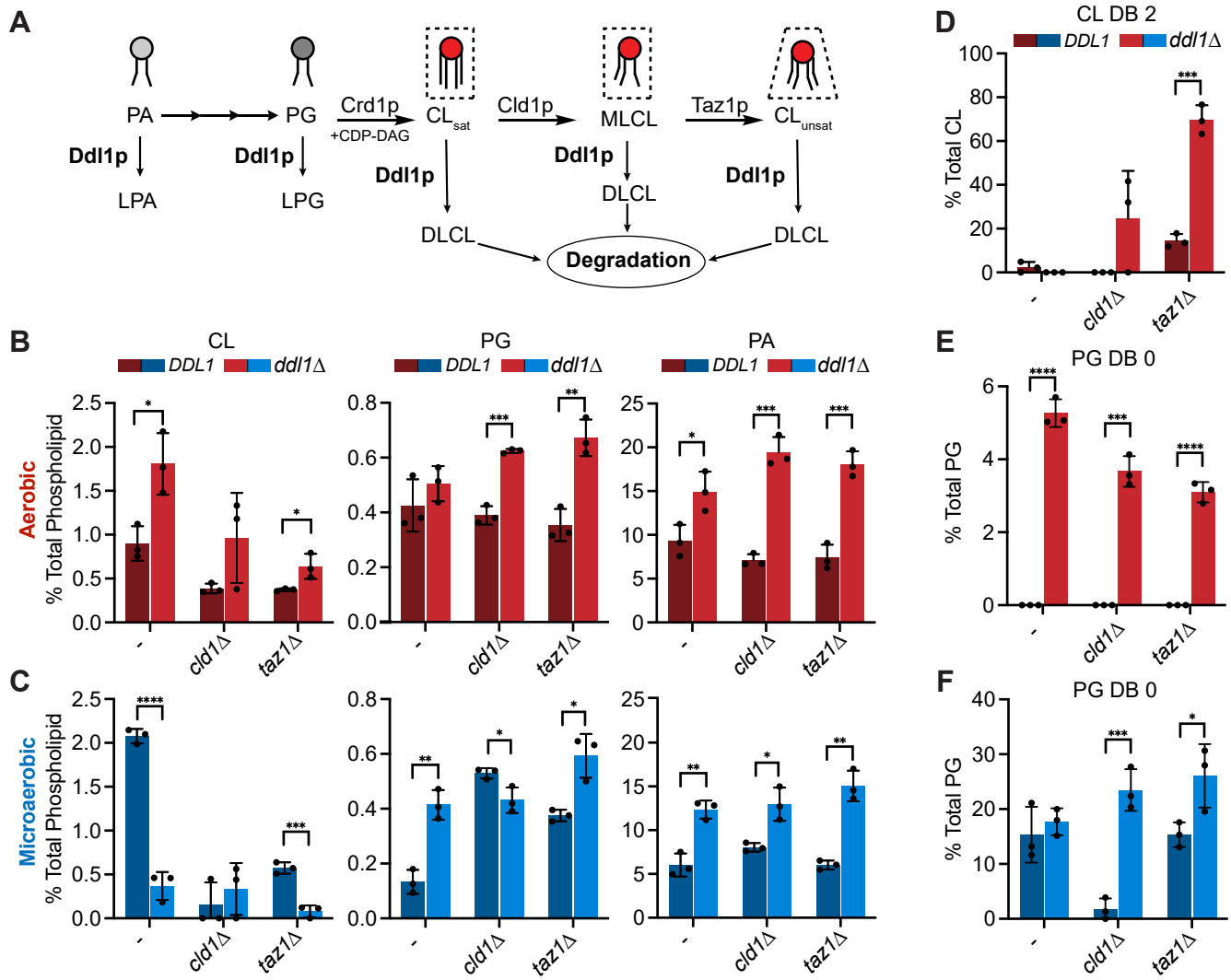


**Fig. 7.** *Ddl1p* activity differentially affects PL metabolism in aerobic and microaerobic conditions. **A:** Schematic depiction of the potential roles of phospholipase A<sub>1</sub> activity in CL biosynthesis and remodeling pathways based on previously observed biochemical activities of *Ddl1p* or its mammalian homologue. *Ddl1p* has been implicated in converting CL precursors PA and PG into lyso-PA (LPA) and lyso-PG (LPG) respectively; and TOCL and MLCL into di-lysocardiolipin (DLCL) which can then be degraded (79). **B:** Loss of *DDL1* in CL remodeling-deficient backgrounds results in increased PA and PG in aerobic conditions, and a smaller increase in CL levels. For all subsequent analyses in this figure: Error bars indicate SD (n = 3) and \**P* < 0.05, \*\**P* < 0.005, \*\*\**P* < 0.001 and \*\*\*\**P* < 0.0001 from unpaired t-tests from each background ± *DDL1*. **C:** Under microaerobic conditions, *ddl1Δ* backgrounds exhibit reduced CL levels, but maintain increases in PG and PA. **D:** Saturated CL (DB 2) appears in remodeling mutants lacking *Ddl1p* grown under aerobic conditions. **E:** Fully saturated PG (DB 0) appears in WT and remodeling mutants lacking *Ddl1p* grown under aerobic conditions. **F:** Fully saturated PG (DB 0) increases only in remodeling mutants lacking *Ddl1p* grown under microaerobic conditions. CL, cardiolipin; MLCL, monolysocardiolipin; PA, phosphatidic acid; PG, phosphatidylglycerol; PL, phospholipid; TOCL, tetraoleoyl (18:1) cardiolipin.

patients (90, 91). However, mitigation of the MLCL:CL ratio through BEL treatment still results in perturbed respiratory capacity in several BTHS models (21, 36, 40). BEL-treated cells have been shown to have large amounts of unremodeled CL (22), similar to *cdl1Δ* yeast. Our results with *cdl1Δ* cells under microaerobic conditions and the combined effects of Palm and BEL-treatment in HEK293 cells support a hypothesis that the accumulation of unremodeled (saturated) CL could act as an additional contributor to mitochondrial dysfunction. If so, availability of exogenous fatty acids might be a key regulator of phenotypes in CL

remodeling mutants. Indeed, previous studies in HeLa cells lacking TAZ have observed a sensitivity of CL and mitochondrial function to changing saturated fatty acid levels (92, 93). Conversely, linoleic acid (18:2) treatment of a BTHS iPSC cardiomyocyte model provided a comparatively greater rescue of mitochondrial functionality than BEL (36), but was less effective in the restoration of cardiac function in a BTHS mouse model (94). Further analyses across a range of systems would be needed to disentangle the individual contributions of MLCL and unremodeled CL to mitochondrial dysfunction. Notably, the analyses performed in this

study do not quantify MLCL, and therefore we cannot preclude its role in phenotypes reported here.


The interplay of CL remodeling, biosynthesis, and potential degradation pathways are another area of future work. We observed that loss of the mitochondrial phospholipase A<sub>1</sub> Dd1lp partially rescued cristae structures in *ddl1Δ* backgrounds under microaerobic growth (Fig. 6). We originally hypothesized that Dd1lp could act to degrade unremodeled CL, leading to the loss of CL in microaerobic *ddl1Δ* cells. While *ddl1Δ* cells showed increased CL levels in aerobic growth (Fig. 7B), they did not under microaerobic conditions (Fig. 7C). However, increased abundance and saturation of PA and PG, which are precursors to CL, were observed in all conditions. One possibility is that the accumulation of saturated PG and PA may prevent CL synthesis under microaerobic conditions, as they are poor substrates for CL synthase and cytidine diphosphate-DAG synthase, respectively (95). We previously observed that high levels of genetically induced lipid saturation increased CL saturation to 1 DB, and drove a 2-fold decrease in its abundance, albeit without an accumulation of PG or PA (55). Interestingly, both CL and PL saturation control the formation of non-lamellar lipid topologies, which are required for optimal tafazzin activity (23), but could also be relevant for the activity of other steps in CL metabolism.

An open question remains why loss of Dd1lp rescues mitochondrial viability under microaerobic conditions. One possibility is that increased levels of the anionic precursors PA or PG might fulfill some of the structural roles of CL. Testing this model would be aided by biochemical analyses of purified mitochondria from microaerobic cells, which currently remains a challenge. Further experiments are also required to better define the phospholipase activity of Dd1lp in cells. The mammalian homologs of Dd1lp, DDHD1/2, have been described as preferentially hydrolyzing PA (96), but activities toward CL have not been reported. Mutations in *DDHD1* cause a subtype of hereditary spastic paraplegia, which specifically exhibits defects in respiratory capacity and increases in oxidative stress (97), raising the possibility that DDHD1 may also alter CL composition, either directly or indirectly through action on CL substrates. In yeast, regulation of Dd1lp might also be involved in the heightened levels of CL we observe under microaerobic conditions. These were surprising given the established correlation between CL synthesis and oxidative phosphorylation components (19) and the lack of change in mitochondrial volume we have previously measured under identical conditions (55). Aerobic *ddl1Δ* cells accumulate CL to similar levels (~2% of a PLs in the cell) as microaerobic WT cells, suggesting that Dd1lp might be responsible for regulating CL levels in response to oxygenation. Previous work has demonstrated that Aft1p, a transcriptional activator that is activated in response to low intracellular iron associated with hypoxia (98), negatively regulates *DDL1*

expression and its deletion causes decreased levels of CL (79). Microaerobic growth could thus lead to activation of Aft1p, repressing *DDL1* expression and increasing CL levels.

Our data support a model that while CL remodeling is dispensable for IMM structure and function in very unsaturated lipid environments, it is likely required to maintain the structure of cristae under conditions of elevated lipid saturation. Both this study and our previous work (55) have demonstrated the sensitivity of CL synthesis and remodeling to changes in the lipidic environment, as both processes become essential for yeast mitochondria under conditions of increased saturation, which has also been alluded to in mammalian cells (93). Such a dynamic could be relevant for understanding the cell-type specific phenotypes of BTHS that arise despite the loss of CL remodeling across a wide range of tissues (99). It could also play a role in the heterogeneity in BTHS pathophysiology observed in populations harboring *TAZ* mutations (99), given the myriad of dietary and metabolic factors that control the composition of circulating and cellular fatty acids. The phenotypes of the remodeling pathway mutants reported here could thus inform the interactions between CL and fatty acid metabolism contributing to mitochondrial dysfunction.

#### Data availability

All data are contained within the article and the [supplemental data](#). All strains and plasmids are available upon request to the corresponding author. 

#### Supplemental data

This article contains [supplemental data](#) (66).

#### Acknowledgments

The authors would like to thank Steven Claypool, Vishal Gohil, Miriam Greenberg, and Budin lab members for their helpful discussions. Steven Claypool generously provided yeast strains. Sterling Ramsey assisted in initial strain development. The UCSD-CMM-EM Core (RRID: SCR\_022039), partly supported by NIH S10OD023527, provided technical assistance and equipment access.

#### Author contributions

K. V. and I. B. writing—original draft; K. V. and I. B. writing—review and editing; K. V. and I. B. conceptualization; K. V. methodology; K. V. investigation; K. V. formal analysis; K. V. data curation; I. B. supervision; I. B. resources; I. B. project administration; I. B. funding acquisition.

#### Author ORCIDs

Kailash Venkatraman  <https://orcid.org/0000-0001-5138-7610>

#### Funding and additional information

The National Institutes of Health (NIH) (R35-GM142960 to I. B.) and the Department of Energy (DE-SC0022954 to I.

B.) provided financial support. K. V. was supported by the NIH Molecular Biophysics Training Grant (T32-GM008326C). Its contents are solely the responsibility of the authors and does not necessarily represent the official views of the National Institutes of Health.

#### Conflict of interest

The authors declare that they have no conflicts of interest within the contents of this article.

#### Abbreviations

BEL, bromoenol lactone; BTHS, Barth syndrome; CL, cardiolipin; CSM, complete supplement mixture; DAG, diacylglycerol; DB, double bond; ER, endoplasmic reticulum; ETC, electron transport chain; iPLA<sub>2</sub>, intracellular phospholipase A<sub>2</sub>; IMM, inner mitochondrial membrane; MLCL, monolysocardiolipin; OA, oleic acid; ORF, open reading frame; Palm, palmitate; PA, phosphatidic acid; PC, phosphatidylcholine; PE, phosphatidylethanolamine; PG, phosphatidylglycerol; PL, phospholipid; PS, phosphatidylserine; ROS, reactive oxygen species; TAZ, tafazzin; TOCL, tetraoleoyl (18:1) cardiolipin.

Manuscript received May 28, 2024, and in revised form July 14, 2024. Published, JLR Papers in Press, July 20, 2024, <https://doi.org/10.1016/j.jlr.2024.100601>

## REFERENCES

1. Acoba, M. G., Senoo, N., and Claypool, S. M. (2020) Phospholipid ebb and flow makes mitochondria go. *J. Cell Biol.* **219**, e202003131
2. Pfeiffer, K., Gohil, V., Stuart, R. A., Hunte, C., Brandt, U., Greenberg, M. L., et al. (2003) Cardiolipin stabilizes respiratory chain supercomplexes. *J. Biol. Chem.* **278**, 52873–52880
3. Gohil, V. M., Hayes, P., Matsuyama, S., Schägger, H., Schlame, M., and Greenberg, M. L. (2004) Cardiolipin biosynthesis and mitochondrial respiratory chain function are interdependent. *J. Biol. Chem.* **279**, 42612–42618
4. Ren, M., Phoon, C. K. L., and Schlame, M. (2014) Metabolism and function of mitochondrial cardiolipin. *Prog. Lipid Res.* **55**, 1–16
5. Paradies, G., Paradies, V., De Benedictis, V., Ruggiero, F. M., and Petrosillo, G. (2014) Functional role of cardiolipin in mitochondrial bioenergetics. *Biochim. Biophys. Acta Bioenerg.* **1837**, 408–417
6. Beltrán-Heredia, E., Tsai, F.-C., Salinas-Almaguer, S., Cao, F. J., Bassereau, P., and Monroy, F. (2019) Membrane curvature induces cardiolipin sorting. *Commun. Biol.* **2**, 225
7. Ikon, N., and Ryan, R. O. (2017) Cardiolipin and mitochondrial cristae organization. *Biochim. Biophys. Acta Biomembr.* **1859**, 1156–1163
8. DeVay, R. M., Dominguez-Ramirez, L., Lackner, L. L., Hoppins, S., Stahlberg, H., and Nunnari, J. (2009) Coassembly of Mgm1 isoforms requires cardiolipin and mediates mitochondrial inner membrane fusion. *J. Cell Biol.* **186**, 793–803
9. Bustillo-Zabalbeitia, I., Montessuit, S., Raemy, E., Basañez, G., Terrones, O., and Martinou, J.-C. (2014) Specific interaction with cardiolipin triggers functional activation of Dynamin-Related Protein 1. *PLoS One* **9**, e102738
10. Stepanyants, N., Macdonald, P. J., Francy, C. A., Mears, J. A., Qi, X., and Ramchandran, R. (2015) Cardiolipin's propensity for phase transition and its reorganization by dynamin-related protein 1 form a basis for mitochondrial membrane fission. *Mol. Biol. Cell* **26**, 3104–3116
11. Dudek, J. (2017) Role of cardiolipin in mitochondrial signaling pathways. *Front. Cell Dev. Biol.* **5**, 90
12. Paradies, G., Paradies, V., Ruggiero, F. M., and Petrosillo, G. (2019) Role of cardiolipin in mitochondrial function and dynamics in health and disease: molecular and pharmacological aspects. *Cells* **8**, 728
13. Hoch, F. L. (1992) Cardiolipins and biomembrane function. *Biochim. Biophys. Acta* **1113**, 71–133

14. Schlame, M., Ren, M., Xu, Y., Greenberg, M. L., and Haller, I. (2005) Molecular symmetry in mitochondrial cardiolipins. *Chem. Phys. Lipids* **138**, 38–49
15. Oemer, G., Koch, J., Wohlfarter, Y., Alam, M. T., Lackner, K., Sailer, S., et al. (2020) Phospholipid acyl chain diversity controls the tissue-specific assembly of mitochondrial cardiolipins. *Cell Rep.* **30**, 4281–4291.e4
16. Pennington, E. R., Funai, K., Brown, D. A., and Shaikh, S. R. (2019) The role of cardiolipin concentration and acyl chain composition on mitochondrial inner membrane molecular organization and function. *Biochim. Biophys. Acta Mol. Cell Biol. Lipids* **1864**, 1039–1052
17. Schlame, M. (2013) Cardiolipin remodeling and the function of tafazzin. *Biochim. Biophys. Acta* **1831**, 582–588
18. Ye, C., Shen, Z., and Greenberg, M. L. (2016) Cardiolipin remodeling: a regulatory hub for modulating cardiolipin metabolism and function. *J. Bioenerg. Biomembr.* **48**, 113–123
19. Xu, Y., Anjaneyulu, M., Donelian, A., Yu, W., Greenberg, M. L., Ren, M., et al. (2019) Assembly of the complexes of oxidative phosphorylation triggers the remodeling of cardiolipin. *Proc. Natl. Acad. Sci. U. S. A.* **116**, 11235–11240
20. Xu, Y., Erdjument-Bromage, H., Phoon, C. K. L., Neubert, T. A., Ren, M., and Schlame, M. (2021) Cardiolipin remodeling enables protein crowding in the inner mitochondrial membrane. *EMBO J.* **40**, e108428
21. Malhotra, A., Edelman-Novemsky, I., Xu, Y., Plesken, H., Ma, J., Schlame, M., et al. (2009) Role of calcium-independent phospholipase A2 in the pathogenesis of Barth syndrome. *Proc. Natl. Acad. Sci. U. S. A.* **106**, 2337–2341
22. Malhotra, A., Xu, Y., Ren, M., and Schlame, M. (2009) Formation of molecular species of mitochondrial cardiolipin. I. A novel transacylation mechanism to shuttle fatty acids between sn-1 and sn-2 positions of multiple phospholipid species. *Biochim. Biophys. Acta* **1791**, 314–320
23. Schlame, M., Acehan, D., Berno, B., Xu, Y., Valvo, S., Ren, M., et al. (2012) The physical state of lipid substrates provides transacylation specificity for tafazzin. *Nat. Chem. Biol.* **8**, 862–869
24. Claypool, S. M., and Koehler, C. M. (2012) The complexity of cardiolipin in health and disease. *Trends Biochem. Sci.* **37**, 32–41
25. Falabella, M., Vernon, H. J., Hanna, M. G., Claypool, S. M., and Pitceathly, R. D. S. (2021) Cardiolipin, mitochondria, and neurological disease. *Trends Endocrinol. Metab.* **32**, 224–237
26. Adès, L. C., Gedeon, A. K., Wilson, M. J., Latham, M., Partington, M. W., Mulley, J. C., et al. (1993) Barth syndrome: clinical features and confirmation of gene localisation to distal Xq28. *Am. J. Med. Genet.* **45**, 327–334
27. Bione, S., D'Adamo, P., Maestrini, E., Gedeon, A. K., Bolhuis, P. A., and Toniolo, D. (1996) A novel X-linked gene, G4.5, is responsible for Barth syndrome. *Nat. Genet.* **12**, 385–389
28. Vreken, P., Valianpour, F., Nijtmans, L. G., Grivell, L. A., Plecko, B., Wanders, R. J., et al. (2000) Defective remodeling of cardiolipin and phosphatidylglycerol in Barth syndrome. *Biochem. Biophys. Res. Commun.* **279**, 378–382
29. Schlame, M., Towbin, J. A., Heerdt, P. M., Jehle, R., DiMauro, S., and Blanck, T. J. J. (2002) Deficiency of tetralinoleoyl-cardiolipin in Barth syndrome. *Ann. Neurol.* **51**, 634–637
30. van Werkhoven, M. A., Thorburn, D. R., Gedeon, A. K., and Pitt, J. J. (2006) Monolysocardiolipin in cultured fibroblasts is a sensitive and specific marker for Barth Syndrome. *J. Lipid Res.* **47**, 2346–2351
31. Byeon, S. K., Ramarajan, M. G., Madugundu, A. K., Oglesbee, D., Vernon, H. J., and Pandey, A. (2021) High-resolution mass spectrometric analysis of cardiolipin profiles in Barth syndrome. *Mitochondrion* **60**, 27–32
32. Barth, P. G., Scholte, H. R., Berden, J. A., Van der Klei-Van Moorsel, J. M., Luyt-Houwen, I. E., Van 't Veer-Korthof, E. T., et al. (1983) An X-linked mitochondrial disease affecting cardiac muscle, skeletal muscle and neutrophil leucocytes. *J. Neurol. Sci.* **62**, 327–355
33. Raja, V., Reynolds, C. A., and Greenberg, M. L. (2017) Barth syndrome: a life-threatening disorder caused by abnormal cardiolipin remodeling. *J. Rare Dis. Res. Treat.* **2**, 58–62
34. Claypool, S. M., McCaffery, J. M., and Koehler, C. M. (2006) Mitochondrial mislocalization and altered assembly of a cluster of Barth syndrome mutant tafazzins. *J. Cell Biol.* **174**, 379–390
35. Acehan, D., Vaz, F., Houtkooper, R. H., James, J., Moore, V., Tokunaga, C., et al. (2011) Cardiac and skeletal muscle defects in a

- mouse model of human Barth syndrome. *J. Biol. Chem.* **286**, 899–908
36. Wang, G., McCain, M. L., Yang, L., He, A., Pasqualini, F. S., Agarwal, A., *et al.* (2014) Modeling the mitochondrial cardiomyopathy of Barth syndrome with induced pluripotent stem cell and heart-on-chip technologies. *Nat. Med.* **20**, 616–623
  37. Pu, W. T. (2022) Experimental models of Barth syndrome. *J. Inherit. Metab. Dis.* **45**, 72–81
  38. Houtkooper, R. H., Rodenburg, R. J., Thiels, C., van Lenthe, H., Stet, F., Poll-The, B. T., *et al.* (2009) Cardiolipin and monolysocardiolipin analysis in fibroblasts, lymphocytes, and tissues using high-performance liquid chromatography-mass spectrometry as a diagnostic test for Barth syndrome. *Anal. Biochem.* **387**, 230–237
  39. Ackermann, E. J., Conde-Frieboes, K., and Dennis, E. A. (1995) Inhibition of macrophage Ca(2+)-independent phospholipase A2 by bromoenol lactone and trifluoromethyl ketones. *J. Biol. Chem.* **270**, 445–450
  40. Anzmann, A. F., Sniezek, O. L., Pado, A., Busa, V., Vaz, F. M., Kreimer, S. D., *et al.* (2021) Diverse mitochondrial abnormalities in a new cellular model of TAFFAZZIN deficiency are remediated by cardiolipin-interacting small molecules. *J. Biol. Chem.* **297**, 101005
  41. Ji, J., and Greenberg, M. L. (2022) Cardiolipin function in the yeast *S. cerevisiae* and the lessons learned for Barth syndrome. *J. Inherit. Metab. Dis.* **45**, 60–71
  42. Beranek, A., Rechberger, G., Knauer, H., Wolinski, H., Kohlwein, S. D., and Leber, R. (2009) Identification of a cardiolipin-specific phospholipase encoded by the gene CLDI (YGR110W) in yeast. *J. Biol. Chem.* **284**, 11572–11578
  43. Abe, M., Hasegawa, Y., Oku, M., Sawada, Y., Tanaka, E., Sakai, Y., *et al.* (2016) Mechanism for remodeling of the acyl chain composition of cardiolipin catalyzed by *Saccharomyces cerevisiae* tafazzin. *J. Biol. Chem.* **291**, 15491–15502
  44. Schlame, M., Xu, Y., and Ren, M. (2017) The basis for acyl specificity in the tafazzin reaction. *J. Biol. Chem.* **292**, 5499–5506
  45. Gu, Z., Valianpour, F., Chen, S., Vaz, F. M., Hakkaart, G. A., Wanders, R. J. A., *et al.* (2004) Aberrant cardiolipin metabolism in the yeast taz1 mutant: a model for Barth syndrome. *Mol. Microbiol.* **51**, 149–158
  46. Claypool, S. M., Whited, K., Srijumngong, S., Han, X., and Koehler, C. M. (2011) Barth syndrome mutations that cause tafazzin complex lability. *J. Cell Biol.* **192**, 447–462
  47. Baile, M. G., Sathappa, M., Lu, Y-W., Pryce, E., Whited, K., Michael McCaffery, J., *et al.* (2014) Unremodeled and remodeled cardiolipin are functionally indistinguishable in yeast. *J. Biol. Chem.* **289**, 1768–1778
  48. Brandner, K., Mick, D. U., Frazier, A. E., Taylor, R. D., Meisinger, C., and Rehling, P. (2005) Taz1, an outer mitochondrial membrane protein, affects stability and assembly of inner membrane protein complexes: implications for Barth Syndrome. *Mol. Biol. Cell.* **16**, 5202–5214
  49. Ye, C., Lou, W., Li, Y., Chatzispayrou, I. A., Hüttemann, M., Lee, I., *et al.* (2014) Deletion of the cardiolipin-specific phospholipase Cld1 rescues growth and life span defects in the tafazzin mutant: implications for Barth syndrome. *J. Biol. Chem.* **289**, 3114–3125
  50. Basu Ball, W., Baker, C. D., Neff, J. K., Apfel, G. L., Lagerborg, K. A., Zun, G., *et al.* (2018) Ethanolamine ameliorates mitochondrial dysfunction in cardiolipin-deficient yeast cells. *J. Biol. Chem.* **293**, 10870–10883
  51. Chen, S., He, Q., and Greenberg, M. L. (2008) Loss of tafazzin in yeast leads to increased oxidative stress during respiratory growth. *Mol. Microbiol.* **68**, 1061–1072
  52. Ma, L., Vaz, F. M., Gu, Z., Wanders, R. J. A., and Greenberg, M. L. (2004) The human TAZ gene complements mitochondrial dysfunction in the yeast taz1Delta mutant. Implications for Barth syndrome. *J. Biol. Chem.* **279**, 44394–44399
  53. Jiang, F., Ryan, M. T., Schlame, M., Zhao, M., Gu, Z., Klingenberg, M., *et al.* (2000) Absence of cardiolipin in the crdl null mutant results in decreased mitochondrial membrane potential and reduced mitochondrial function. *J. Biol. Chem.* **275**, 22387–22394
  54. Baile, M. G., Whited, K., and Claypool, S. M. (2013) Deacylation on the matrix side of the mitochondrial inner membrane regulates cardiolipin remodeling. *Mol. Biol. Cell.* **24**, 2008–2020
  55. Venkatraman, K., Lee, C. T., Garcia, G. C., Mahapatra, A., Milshteyn, D., Perkins, G., *et al.* (2023) Cristae formation is a mechanical buckling event controlled by the inner mitochondrial membrane lipidome. *EMBO J.* **42**, e114054
  56. Kwast, K. E., Burke, P. V., Staahl, B. T., and Poyton, R. O. (1999) Oxygen sensing in yeast: evidence for the involvement of the respiratory chain in regulating the transcription of a subset of hypoxic genes. *Proc. Nat. Acad. Sci. U. S. A.* **96**, 5446–5451
  57. Vasconcelles, M. J., Jiang, Y., McDaid, K., Gilooly, L., Wretzel, S., Porter, D. L., *et al.* (2001) Identification and characterization of a low oxygen response element involved in the hypoxic induction of a family of *Saccharomyces cerevisiae* genes. *J. Biol. Chem.* **276**, 14374–14384
  58. [preprint] Wong, A. M., and Budin, I. (2024) Organelle-targeted Laurdans measure heterogeneity in subcellular membranes and their responses to saturated lipid stress. *bioRxiv*. <https://doi.org/10.1101/2024.04.16.589828>
  59. Ståhlman, M., Ejsing, C. S., Tarasov, K., Perman, J., Borén, J., and Ekroos, K. (2009) High-throughput shotgun lipidomics by quadrupole time-of-flight mass spectrometry. *J. Chromatogr. B.* **877**, 2664–2672
  60. Klose, C., Surma, M. A., Gerl, M. J., Meyenhofer, F., Shevchenko, A., and Simons, K. (2012) Flexibility of a eukaryotic lipidome – insights from yeast lipidomics. *PLoS One* **7**, e35063
  61. Ejsing, C. S., Sampaio, J. L., Surendranath, V., Duchoslav, E., Ekroos, K., Klemm, R. W., *et al.* (2009) Global analysis of the yeast lipidome by quantitative shotgun mass spectrometry. *Proc. Nat. Acad. Sci. U. S. A.* **106**, 2136–2141
  62. Surma, M. A., Herzog, R., Vasili, A., Klose, C., Christinat, N., Morin-Rivron, D., *et al.* (2015) An automated shotgun lipidomics platform for high throughput, comprehensive, and quantitative analysis of blood plasma intact lipids. *Eur. J. Lipid Sci. Technol.* **117**, 1540–1549
  63. Herzog, R., Schwudke, D., Schuhmann, K., Sampaio, J. L., Bornstein, S. R., Schroeder, M., *et al.* (2011) A novel informatics concept for high-throughput shotgun lipidomics based on the molecular fragmentation query language. *Genome Biol.* **12**, R8
  64. Herzog, R., Schuhmann, K., Schwudke, D., Sampaio, J. L., Bornstein, S. R., Schroeder, M., *et al.* (2012) LipidXplorer: a software for consensual cross-platform lipidomics. *PLoS One* **7**, e29851
  65. Fuhrmann, D. C., and Brüne, B. (2017) Mitochondrial composition and function under the control of hypoxia. *Redox Biol.* **12**, 208–215
  66. Degreif, D., de Rond, T., Bertl, A., Keasling, J. D., and Budin, I. (2017) Lipid engineering reveals regulatory roles for membrane fluidity in yeast flocculation and oxygen-limited growth. *Metab. Eng.* **41**, 46–56
  67. Klecker, T., and Westermann, B. (2021) Pathways shaping the mitochondrial inner membrane. *Open Biol.* **11**, 210238
  68. Kamphorst, J. J., Cross, J. R., Fan, J., de Stanchina, E., Mathew, R., White, E. P., *et al.* (2013) Hypoxic and Ras-transformed cells support growth by scavenging unsaturated fatty acids from lysophospholipids. *Proc. Natl. Acad. Sci. U. S. A.* **110**, 8882–8887
  69. Ackerman, D., Tumanov, S., Qiu, B., Michalopoulou, E., Spata, M., Azzam, A., *et al.* (2018) Triglycerides promote lipid Homeostasis during hypoxic stress by balancing fatty acid saturation. *Cell Rep.* **24**, 2596–2605.e5
  70. Ban-Ishihara, R., Ishihara, T., Sasaki, N., Mihara, K., and Ishihara, N. (2013) Dynamics of nucleoid structure regulated by mitochondrial fission contributes to cristae reformation and release of cytochrome c. *Proc. Nat. Acad. Sci. U. S. A.* **110**, 11863–11868
  71. Ishihara, T., Ban-Ishihara, R., Ota, A., and Ishihara, N. (2022) Mitochondrial nucleoid trafficking regulated by the inner-membrane AAA-ATPase ATAD3A modulates respiratory complex formation. *Proc. Nat. Acad. Sci. U. S. A.* **119**, e2210730119
  72. Mthembu, S. X. H., Mazibuko-Mbeje, S. E., Silvestri, S., Orlando, P., Marcheggiani, F., Cirilli, I., *et al.* (2024) Low levels and partial exposure to palmitic acid improves mitochondrial function and the oxidative status of cultured cardiomyoblasts. *Toxicol. Rep.* **12**, 234–243
  73. Hsu, P., Liu, X., Zhang, J., Wang, H-G., Ye, J-M., and Shi, Y. (2015) Cardiolipin remodeling by TAZ/tafazzin is selectively required for the initiation of mitophagy. *Autophagy* **11**, 643–652
  74. Shen, Z., Li, Y., Gasparski, A. N., Abeliovich, H., and Greenberg, M. L. (2017) Cardiolipin regulates mitophagy through the protein kinase C pathway. *J. Biol. Chem.* **292**, 2916–2923
  75. Sakakibara, K., Eiyama, A., Suzuki, S. W., Sakoh-Nakatogawa, M., Okumura, N., Tani, M., *et al.* (2015) Phospholipid methylation



- controls Atg32-mediated mitophagy and Atg8 recycling. *EMBO J.* **34**, 2703–2719
76. Kanki, T., Wang, K., Cao, Y., Baba, M., and Klionsky, D. J. (2009) Atg32 is a mitochondrial protein that confers selectivity during mitophagy. *Dev. Cell.* **17**, 98–109
  77. Xu, Y., Phoon, C. K. L., Berno, B., D'Souza, K., Hoedt, E., Zhang, G., *et al.* (2016) Loss of protein association causes cardiolipin degradation in Barth syndrome. *Nat. Chem. Biol.* **12**, 641–647
  78. Urafuji, K., and Arioka, M. (2016) Yor022c protein is a phospholipase A1 that localizes to the mitochondrial matrix. *Biochem. Biophys. Res. Commun.* **480**, 302–308
  79. Yadav, P. K., and Rajasekharan, R. (2016) Misregulation of a DDHD domain-containing lipase causes mitochondrial dysfunction in yeast. *J. Biol. Chem.* **291**, 18562–18581
  80. Rand, R. P., and Sengupta, S. (1972) Cardiolipin forms hexagonal structures with divalent cations. *Biochim. Biophys. Acta.* **255**, 484–492
  81. Cullis, P. R., Verkleij, A. J., and Ververgaert, P. H. (1978) Polymorphic phase behaviour of cardiolipin as detected by 31P NMR and freeze-fracture techniques. Effects of calcium, dibucaine and chlorpromazine. *Biochim. Biophys. Acta.* **513**, 11–20
  82. Lewis, R. N. A. H., and McElhane, R. N. (2009) The physicochemical properties of cardiolipin bilayers and cardiolipin-containing lipid membranes. *Biochim. Biophys. Acta.* **1788**, 2069–2079
  83. Lewis, R. N. A. H., Zweytick, D., Pabst, G., Lohner, K., and McElhane, R. N. (2007) Calorimetric, x-ray diffraction, and spectroscopic studies of the thermotropic phase behavior and organization of tetramyristoyl cardiolipin membranes. *Biophys. J.* **92**, 3166–3177
  84. Barbot, M., Jans, D. C., Schulz, C., Denkert, N., Kroppen, B., Hoppert, M., *et al.* (2015) Mic10 oligomerizes to bend mitochondrial inner membranes at cristae junctions. *Cell Metab.* **21**, 756–763
  85. Tarasenko, D., Barbot, M., Jans, D. C., Kroppen, B., Sadowski, B., Heim, G., *et al.* (2017) The MICOS component Mic60 displays a conserved membrane-bending activity that is necessary for normal cristae morphology. *J. Cell Biol.* **216**, 889–899
  86. Blum, T. B., Hahn, A., Meier, T., Davies, K. M., and Kühlbrandt, W. (2019) Dimers of mitochondrial ATP synthase induce membrane curvature and self-assemble into rows. *Proc. Natl. Acad. Sci. U. S. A.* **116**, 4250–4255
  87. Powell, G. L., and Marsh, D. (1985) Polymorphic phase behavior of cardiolipin derivatives studied by phosphorus-31 NMR and x-ray diffraction. *Biochemistry.* **24**, 2902–2908
  88. Boyd, K. J., Alder, N. N., and May, E. R. (2018) Molecular dynamics analysis of cardiolipin and monolysocardiolipin on bilayer properties. *Biophys. J.* **114**, 2116–2127
  89. Duncan, A. L. (2020) Monolysocardiolipin (MLCL) interactions with mitochondrial membrane proteins. *Biochem. Soc. Trans.* **48**, 993–1004
  90. Valianpour, F., Mitsakos, V., Schlemmer, D., Towbin, J. A., Taylor, J. M., Ekert, P. G., *et al.* (2005) Monolysocardiolipins accumulate in Barth syndrome but do not lead to enhanced apoptosis. *J. Lipid Res.* **46**, 1182–1195
  91. Saric, A., Andreau, K., Armand, A-S., Møller, I. M., and Petit, P. X. (2015) Barth syndrome: from mitochondrial dysfunctions associated with aberrant production of reactive oxygen species to pluripotent stem cell studies. *Front. Genet.* **6**, 359
  92. Oemer, G., Edenhofer, M-L., Wohlfarter, Y., Lackner, K., Leman, G., Koch, J., *et al.* (2021) Fatty acyl availability modulates cardiolipin composition and alters mitochondrial function in HeLa cells. *J. Lipid Res.* **62**, 100111
  93. Oemer, G., Koch, J., Wohlfarter, Y., Lackner, K., Gebert, R. E. M., Geley, S., *et al.* (2022) The lipid environment modulates cardiolipin and phospholipid constitution in wild type and tafazzin-deficient cells. *J. Inherit. Metab. Dis.* **45**, 38–50
  94. Zhu, S., Pang, Y., Nguyen, A., Huynh, H., Lee, S., Gu, Y., *et al.* (2024) Dietary linoleic acid supplementation fails to rescue established cardiomyopathy in Barth syndrome. *J. Mol. Cell Cardiol. Plus.* **8**, 100076
  95. Ostrander, D. B., Sparagna, G. C., Amoscato, A. A., McMillin, J. B., and Dowhan, W. (2001) Decreased cardiolipin synthesis corresponds with cytochrome c release in palmitate-induced cardiomyocyte apoptosis. *J. Biol. Chem.* **276**, 38061–38067
  96. Higgs, H. N., and Glomset, J. A. (1996) Purification and properties of a phosphatidic acid-preferring phospholipase A1 from bovine testis. Examination of the molecular basis of its activation. *J. Biol. Chem.* **271**, 10874–10883
  97. Tesson, C., Nawara, M., Salih, M. A. M., Rossignol, R., Zaki, M. S., Al Balwi, M., *et al.* (2012) Alteration of fatty-acid-metabolizing enzymes affects mitochondrial form and function in hereditary spastic paraplegia. *Am. J. Hum. Genet.* **91**, 1051–1064
  98. Yamaguchi-Iwai, Y., Dancis, A., and Klausner, R. D. (1995) AFT1: a mediator of iron regulated transcriptional control in *Saccharomyces cerevisiae*. *EMBO J.* **14**, 1231–1239
  99. Clarke, S. L. N., Bowron, A., Gonzalez, I. L., Groves, S. J., Newbury-Ecob, R., Clayton, N., *et al.* (2013) Barth syndrome. *Orphanet J. Rare Dis.* **8**, 23